ELECTROCHEMICALLY EXFOLIATED GRAPHENE PRODUCTION BY USING PURE GRAPHITE AND PENCIL CORE

Emrah Bulut[1]*

[1]Sakarya University, Department of Chemistry

Abstract: Under the scope of this study, graphene sheets were produced with different graphite precursors by electrochemical exfoliation technique as an environmentally friendly approach. Pure graphite and pencil core with different grade were used as a precursor material (working electrode). A Pt wire and Ag/AgCl were used as counter and reference electrode, respectively. Electrodes were immersed into H_2SO_4 electrolyte solution. The resultant electrochemically exfoliated graphene sheets (EGS) were dispersed in N,N-dimethylformamide (DMF) by sonication at low power for 10 min. Structural analysis of as obtained EGS were performed by Fourier Transform Infrared (FTIR) spectroscopy, Raman spectroscopy, and X-Ray Diffraction (XRD) spectroscopy. Microscopic structure of the pre- and post-production of graphite and as obtained graphene sheets were investigated by Field Emission Scanning Electron Microscopy (FE-SEM). The purity of the graphene sheets was identified qualitatively by Electron Diffraction spectroscopy (EDS).

Keywords: A few layered graphene, Electrochemical exfoliation, Pencil core.

Corresponding author. E-mail: ebulut@sakarya.edu.tr

INTRODUCTION

Nanostructured materials, as compared with bulk materials, are seen to exhibit improved performance (1). One of the most unique products of nanotechnology is graphene. Graphene is an emerging class of ultrathin carbon membrane materials with high electrical and thermal conductivity, specific surface area, elasticity, and chemical stability.

Graphene is an only one atom-thick, mono-layered, and 2 dimensional sp^2 carbon lattice. It has exceptional properties, such as elastic modulus of up to 1 TPa, electrical conductivity of up to 104 S/cm and surface area of over 2500 m^2/g. These superior physicochemical properties have inspired applications in electronics (2), conductive composites (3), catalysis (4), photovoltaics (5), energy storage (6), and biology (7,8).

The number of the methods that can be used to obtain graphene is limited. These methods can be sorted as Chemical Vapor Deposition (CVD) (9), ultrasonic exfoliation of graphite (10), epitaxial growth on nonconductive surfaces (11), Hummers (12) and electrochemical exfoliation of graphite (13-15). Of these, the most widely used is Hummers method. In this method, primarily, graphite is oxidized to the graphene oxide then it is reduced to the graphene sheets. However, this method requires large volumes of chemicals, also intermediate processes take too much time.

Electrochemical method is another approach for the exfoliation of graphite. Compared to the other methods, it is more controllable and causes less defect. In suitable electrolytes, graphite electrodes were intercalated to give graphene intercalation compounds by adjusting the driving potential, and then exfoliated by solvent decomposition directly during electrochemical treatment (16). This study will also contribute to the production of cheap graphene in the literature.

MATERIALS AND METHODS

Environmentally benign production of graphene was achieved through the electrochemical exfoliation by using different graphite sources. Pure graphite rods and pencil leads with different hardnesses were used as graphite sources and also the working electrode. Platinum wire and Ag/AgCl electrode were used as counter and reference electrode, respectively. All electrodes were immersed to the 0,1 M H_2SO_4 solution which was the electrolyte in this study. 5 V electrical potential was applied for 10 minutes to the electrolytic cell. Thus obtained graphene sheets were filtered and washed then ultrasonically dispersed in N,N-dimethylformamide. A few drops of the dispersion were dried on a glass substrate for characterization.

For the structural analysis of the synthesized graphene sheets, Fourier Transform Infrared (FTIR) Spectroscopy, Raman Spectroscopy and X-Ray Diffraction (XRD) Spectroscopy were utilized. FTIR measurement was performed using a Perkin Elmer Spectrum Two spectrometer. XRD spectrometer (Rigaku D/Max 2200) equipped with graphite monochromatized Cu Kα radiation (λ=1.5406 Å). The operation voltage and current were 40 kV and 40 mA, respectively. The diffracted intensities were recorded from 10° to 50°, 2θ angles. The morphological characterizations were performed by scanning electron microscopes (field emission FE-SEM: FEI Quanta FEG 450 and SEM: JEOL JSM-6060 LV).

RESULTS AND DISCUSSION

Graphene sheets were primarily analyzed by XRD. Figure 1 shows XRD patterns of the as produced graphene powder and graphite rod. The peak at around 2θ=26,6° belongs to the (002) diffraction (17). This peak was derived from repetitive interlayer structure of graphite. However, it disappeared at graphene pattern due to the intercalation of graphite structure. Disappearance of this peak showed that graphite has decomposed to the graphene sheets. Also, similar XRD patterns obtained for the pencil core before and after the exfoliation.

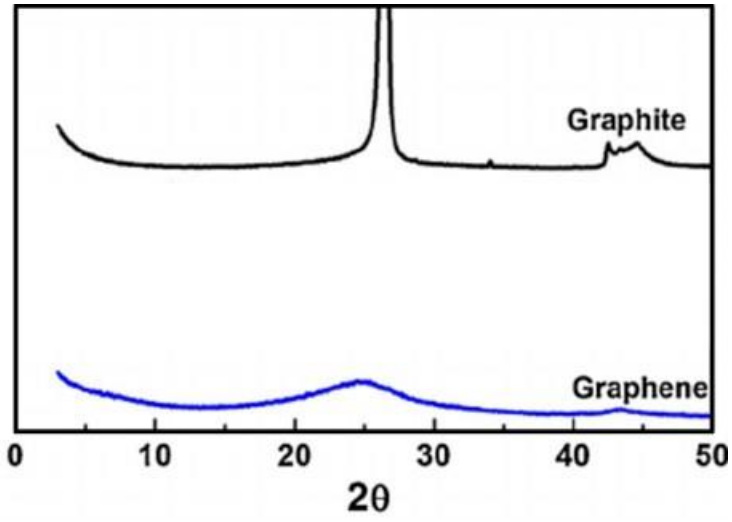

Figure 1: XRD patterns of graphite and graphene

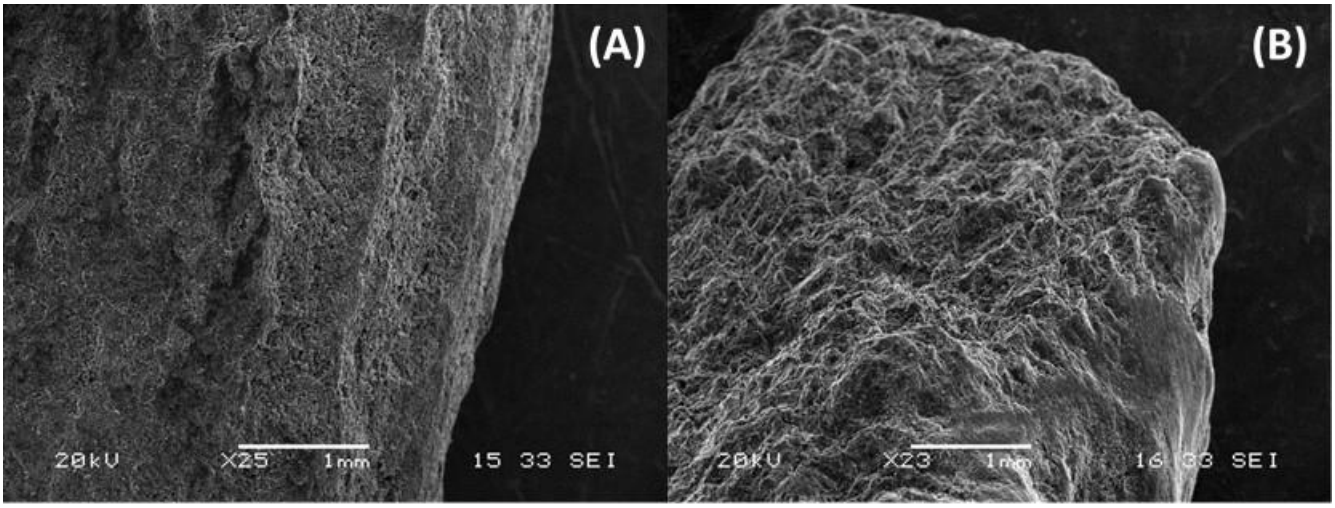

Figure 2: FE-SEM images of the graphene sheets.

FE-SEM images of the graphene sheets, produced from graphite rod and pencil core by electrochemical exfoliation, were shown in Figures 2, 3, and 4. Figure 2 A and B show the block type morphology of the graphite rod and pencil core, respectively, before electrochemical exfoliation.

Interlayers of the graphene can be seen in Figure 3 very clearly. In addition, a few layered graphene sheet was shown in Figure 4. As seen on the figures, the production of a few layered graphene was proved to be successful.

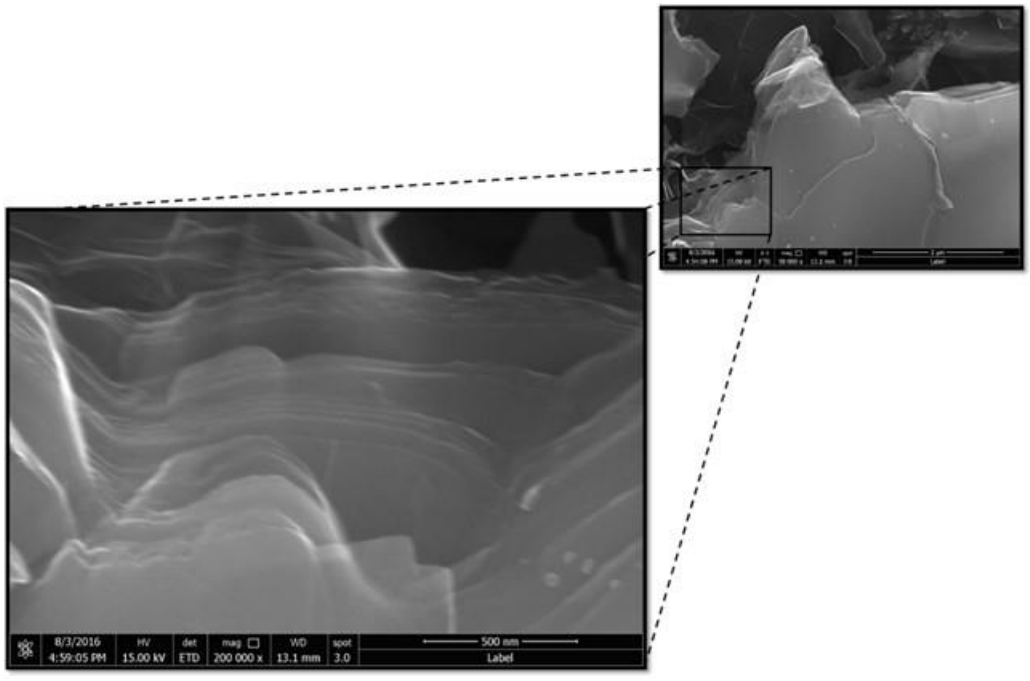

Figure 3: FE-SEM images of graphene interlayers (200000 x).

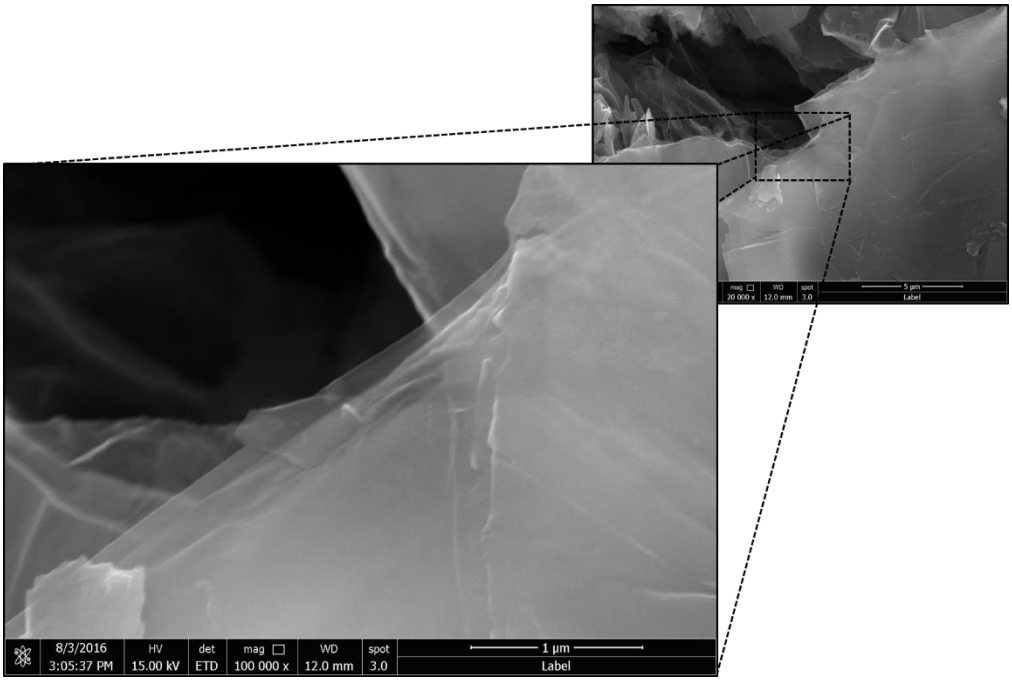

Figure 4: FE-SEM images of a few layered graphene sheet.

Molecular structures of working electrodes and as produced graphene sheets were examined by attenuated total reflection (ATR-FTIR). Pencil core used as graphite source was compared with pure graphite rod. FTIR spectra of the both are very similar. However, there are some different bands in pencil core spectrum due to clay and wax, which are mixed and immersed into pencil during the production.

Figure 5 shows the FTIR spectra of pencil core and pure graphene. The spectrum of the pencil core exhibits absorption bands at 2954, 2921, 2855 cm^{-1} representing the symmetric and asymmetric CH, CH_2, CH_3 stretching modes. 1376 and 1459 cm^{-1} bands corresponding to the CH_2 and CH_3 deformations. The band at around 1640 cm^{-1} originates from the presence of C≡C bonds (18). Also the peak around 1700 cm^{-1} indicates the C-O derivatives and caused by the wax existing in pencil core content. Bands around 1100 cm^{-1} can be assigned to the Si-O derivatives in the clay which is a component of pencil core. We observed that the components of the pencil core, like clay and wax, have no negative effect on the production of graphene.

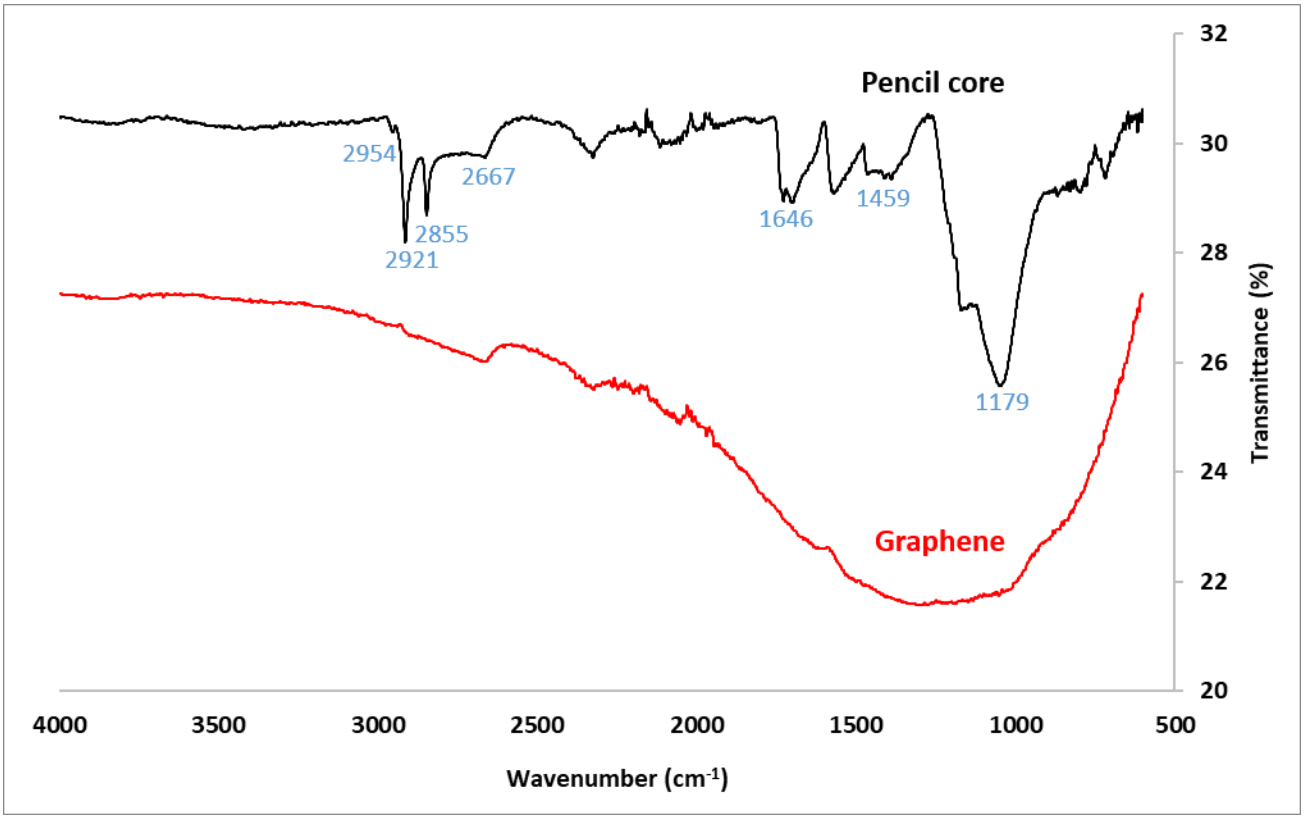

Figure 5: FTIR spectra of pencil core and pure graphene.

The absence of C-O and –OH derivatives in the FTIR spectrum of graphene confirms the low oxidation degree of the graphene sheets.

The presence of graphene, number of graphene layers, defects on graphene sheets and crystallinity can be determined influentially by Raman spectroscopy. There are three significant bands in the Raman spectrum: D (defect) band, G (vibrations of sp^2 carbon atoms on graphene layer), and 2D (second harmonic of the D band) band. Also D' band can be observed as a shoulder on G band. D and D' bands are relevant with presence of structural defects on graphene and graphite. The I_D/I_G ratio is often used to determine the quality of the graphene.

In the Raman spectrum of the electrochemically exfoliated graphene (Figure 6), ~2710 and ~1586 cm^{-1} bands correspond to the 2D and G bands, respectively. Also defect D band was observed at ~1348 cm^{-1}. Intensity ratio of D and G bands (I_D/I_G) is 0,54. This value is much lower than that of thermally (1,5) and chemically (1,2) reduced graphene (19-20).

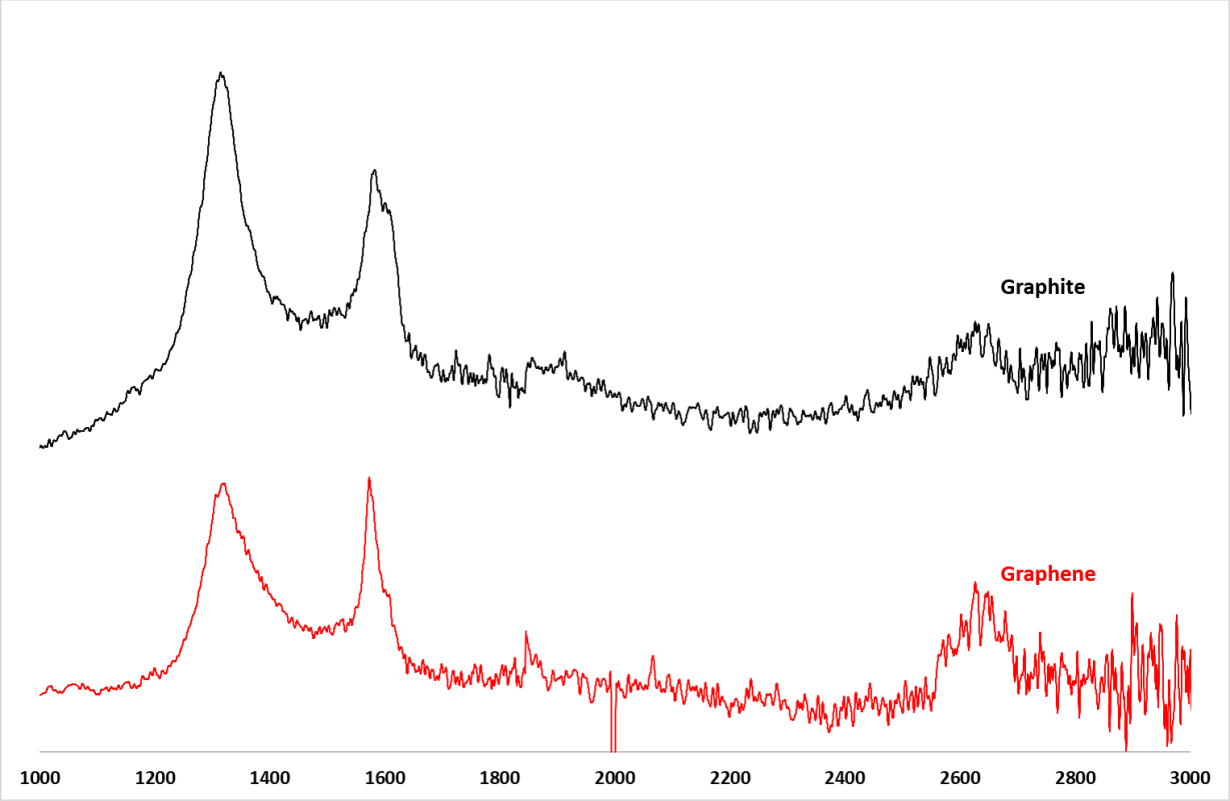

Figure 6: Raman spectra of graphite and graphene.

CONCLUSIONS

In this work, we evaluated the utilization of electrochemically exfoliated graphene from pencil core and pure graphite. A simple, greener, rapid, and cost-effective electrochemical method for the synthesis of GO and GNs from pencil is demonstrated at room temperature is achieved. The prepared graphene nanosheets was characterized by FE-SEM, XRD, FTIR, and Raman spectroscopy and these confirmed the formation of a few layered graphene nanosheets with fewer defects. Moreover, due to the simplicity of this method for the synthesis of graphene nanosheets, it may find promising applications in more areas.

ACKNOWLEDGMENTS

This work was supported by The Scientific and Technological Research Council of Turkiye, under Grant Number of 315M250.

REFERENCES

1. Shukla A, Kumar T. Materials for next-generation lithium batteries. Current Science. 2008;94:314-31.
2. Schwierz F. Graphene transistors. Nature Nanotechnology. 2010;5:487-96.

3. Stankovich SD, Dikin A, Dommett GHB, Kohlhaas KM, Zimney EJ, Stach EA, Piner RD, Nguyen ST, Ruoff RS. Graphene-based composite materials. Nature. 2006;442:282-86.

4. Chen D, Tang LH, Li JH. Graphene-based materials in electrochemistry. Chemical Society Reviews. 2010;39:3157-80.

5. Guo CX, Yang HB, Sheng ZM, Lu ZS, Song QL, Li CM. Layered graphene/quantum dots for photovoltaic devices. Angewandte Chemie. 2010;49:3014-17.

6. Yoo JJK, Balakrishnan JS, Huang V, Meunier BG, Sumpter A, Srivastava M, Conway ALM, Reddy JY, Vajtai R. Ultrathin Planar Graphene Supercapacitors. Nano Letters. 2011;11:1423-27.

7. He SJB, Song D, Li CF, Zhu WP, Qi YQ, Wen LH, Wang SP, Song HP, Fan CHA. A graphene nanoprobe for rapid, sensitive, and multicolor fluorescent DNA analysis. Advanced Functional Materials. 2010;20:453-59.

8. Worsley MA, Thang T. Synthesis and characterization of highly crystalline graphene aerogels. ACS Nano. 2014;8:11013-22.

9. Mattevi, C, Kim H, Chhowalla M. A review of chemical vapour deposition of graphene on copper. Journal of Materials Chemistry. 2011;21:3324-34.

10. Hernandez Y. High-yield production of graphene by liquid-phase exfoliation of graphite. Nature Nanotechnology. 2008;3:563-68.

11. Strupinski W. Graphene epitaxy by chemical vapor deposition on SiC. Nano Letters. 2011;11:1786-91.

12. Hummers WS, Offeman RE. Preparation of graphitic oxide. Journal of American Chemical Society.1958;80:1339-39.

13. Bourelle E. Electrochemical exfoliation of HOPG in formic - sulfuric acid mixtures. Molecular Crystals and Liquid Crystals. 1998;310:321-26.

14. Liu N, Luo F, Wu H, Liu Y, Zhang C, Chen J. One-step ionic-liquid-assisted electrochemical synthesis of ionic-liquid-functionalized graphene sheets directly from graphite. Advanced Functional Materials. 2008;18:1518-25.

15. Xia ZY. The exfoliation of graphene in liquids by electrochemical, chemical, and sonication-assisted techniques: A nanoscale study. Advanced Functional Materials. 2013;23:4684-93.

16. Su CY. High-quality thin graphene films from fast electrochemical exfoliation. ACS Nano. 2011;5:2332-39.

17. Abdelkader, A.M., Kinloch, I.A., Dryfe, R.A.W., Continuous Electrochemical Exfoliation of Micrometer-Sized Graphene Using Synergistic Ion Intercalations and Organic Solvents, ACS Appl. Mater. Interfaces, 2014;6:1632−1639.

18. Pavithra, C.L.P., Sarada, B.V., et.al., Synthesis of Copper-Graphene Nanocomposite Foils with High Hardness, Sci. Reports, 2014;4:4049.

19. Park S, Rouff RS. Chemical methods for the production of graphenes. Nature Nanotechnology. 2009;4:217-24.

20. Mattevi C, Eda G, Agnoli S, Miller S, Mkhoyan KA, Celik O, Mastrogiovanni D, Granozzi G, Garfunkel E, Chhowalla M. Evolution of electrical, chemical, and structural properties of transparent and conducting chemically derived graphene thin films. Advanced Functional Materials. 2009;19:2577-83.

JOTCS B
Journal of the Turkish Chemical Society
Section: B
Chemical Engineering
TURKISH CHEMICAL SOCIETY

REMOVAL OF ACETIC ACID FROM DILUTE AQUEOUS SOLUTIONS USING ZEOLITE 13X

Güler NARİN

Uşak University, Faculty of Engineering, Department of Chemical Engineering, 64200 Uşak, Turkey

Abstract: In this study, acetic acid adsorption equilibrium and kinetics of 13X synthetic zeolite from aqueous solutions at 25, 35 and 45 °C were investigated. 13X particles (particle diameter in the range of 75–150 μm) were contacted with different initial acetic acid cocentrations in aqueous phases (0.2–3 wt. %) at constant temperature in a batch reactor. Acetic acid concentrations of the liquid samples taken from the adsorption mixtures at specific time intervals were measured by titration with NaOH solution and the time required for the system to reach equilibrium and acetic acid amounts adsorbed at equilibrium were determined. The experimental adsorption kinetics data was best represented by the pseudo-second order model and the model parameters were calculated. The experimental equilibrium data was fitted to the Sips model and the model parameters were calculated. Adsorption thermodynamic parameters (standard Gibbs free energy change, enthalpy change, and entropy change of adsorption) were determined. The acetic acid-saturated adsorbent was regenerated by two methods in order to evaluate its reusability. Adsorption of acetic acid on 13X led to appearance of new bands in at 1390, 1472 and 1593 cm^{-1} in the transmittance infrared spectrum which were assigned to the acetate ions. Regeneration of the acetic acid-saturated 13X in deionized water at 45 °C led to loss in intensities of these bands indicating dissolution of the weakly adsorbed species associated with these bands. After heating at 300 °C, the bands at 1472 and 1593 cm^{-1} disappeared whereas 1390 cm^{-1} band remained and a very weak shoulder band appeared at 1720 cm^{-1}.

Keywords: Synthetic zeolite, acetic acid, adsorption, equilibrium, kinetics, modelling.

Submitted: April 13, 2017**. Accepted:** September 28, 2017**.**

Cite this: Narin G. REMOVAL OF ACETIC ACID FROM DILUTE AQUEOUS SOLUTIONS USING ZEOLITE 13X. JOTCSB. 2017;1(2):159–90.

***Corresponding author. E-mail:** guler.narin@usak.edu.tr.

INTRODUCTION

Acetic acid is one of the most important chemicals in the chemical industry and belongs to the top 50 chemicals in amount produced (1). Acetic acid is used in the manufacture of vinyl acetate, acetic anhydride, acetate esters, monochloroacetic acid, and as a solvent in the production of dimethyl terephthalate and terephthalic acid (2). Worldwide acetic acid production between 2009 and 2014 had grown by an average of 3–4% per year, while world acetic acid capacity had grown by an average of 4% per year. In 2010 world capacity exceeded 12 million tons/year (2). On an industrial scale acetic acid is produced via the petrochemical route: Carbonylation of methanol, liquid-phase oxidation of hydrocarbons, and oxidation of acetaldehyde (3). By 2012 *ca.* 90% of acetic acid is manufactured by low-pressure methanol carbonylation technologies (2). In this process, methanol and carbon monoxide are reacted in the liquid phase, with some water to keep the catalyst in solution. After the reaction, a distillation column is employed to remove methanol, water and carbon monoxide (4).

Gradual depletion of petroleum reserves, increasing prices of petrochemical feedstocks as well as environmental concerns have led to a search for alternative carboxylic acid production methods such as fermentation of biomass, forestry residues, municipal wastes, and other byproducts (5, 6). The acetic acid produced by fermentation is in dilute aqueous solutions, usually lower than 5 wt. % (7), so that its purification involves separation of acetic acid from a large quantity of water. The cost of such separation accounts more than half of the total production cost (8).

The increasing demand for acetic acid has led to an increase in the acetic acid amount in the industrial wastewaters. Acids in wastewater are classified as priority pollutants and they must be recycled, diluted or treated chemically and then degraded biologically. European countries require neutralization or biological degradation of these waste streams (2).

Acetic acid concentrations in the waste streams and fermentation broths are usually lower than 5 wt. % (9-12). Separation of carboxylic acids from aqueous solution is necessary in petrochemical manufacture, fermentation, and the environmentally and economically important recovery from waste streams (13). The selection of an acetic acid separation method depends on the economics. The conventional industrial method of carboxylic acid separation from the fermentation broth is precipitation using calcium hydroxide. However this separation process requires large amounts of sulfuric acid and generates solid waste in the form of calcium sulfate. Conventional distillation is energy-intensive due to the small differences in the volatilities of water and acetic acid. This separation process is economically viable provided that the acetic acid is highly concentrated (1, 14, 15) at concentrations exceeding 70 wt. % (3).

For separation of acetic acid from the dilute solutions, various other methods have been investigated in recent years including solvent extraction (16), reactive extraction (10, 17-20), pervaporation (14, 21-34) and electrodialysis (35-38). However most of these methods have drawbacks such as high capital costs, low efficiency, complexity of operation, high chemical and energy consumption as well as adverse environmental impact (39, 40).

Adsorptive separations can provide a viable option for separation of acetic acid from the dilute aqueous solutions (41). The adsorption process allows flexibility in terms of both design and operation. After adsorption, the adsorbent should be easily regenerated, thereby resulting in significant cost savings. Activated carbons (15, 41-48), basic polymeric adsorbents (42, 45, 49-51), ion exchangers (17, 52), silica gel (53), clays (54, 55), and carbon nanotubes (56) were investigated as adsorbents for removal of acetic acid from the dilute aqueous solutions. Synthetic zeolites (55, 57-60) and metal organic frameworks (61) are other adsorbents tested recently for the adsorptive separation of acetic acid/water.

Pervaporation has attracted increasing attention as an effective and energy-efficient technique for the separation of azeotrope or close-boiling liquid mixtures (62-65). Zeolite membranes have advantages over polymer membranes due to their better chemical and thermal stability. In general, hydrophilic zeolite membranes have been used for dehydration of organic solvents (66-68), while hydrophobic zeolite membranes have been used for separation of organics from water (14, 27, 66, 69, 70). Zeolite membranes have examined for separation of acetic acid-water mixtures by pervaporation (14, 22, 26, 29, 34).

An energy-efficient cyclic process has been patented for the simultaneous removal and recovery of acetic acid from water by concentration swing adsorption based on activated carbon adsorbent. In this process the more adsorbable component is acetic acid, the less adsorbable component is water, and the desorbent liquid is acetone (15).

The design and optimization of such a cyclic adsorptive separation process require determination of the adsorption equilibrium and kinetic parameters. Furthermore, the ideal adsorbent should have high adsorption capacity and selectivity, and be low-cost, easy to handle, environmentally neutral, non-toxic, and easy to regenerate.

In the present study equilibrium and kinetics of adsorption of acetic acid on 13X was studied. Several adsorption equilibrium and kinetic models were used to correlate the experimental data. From the adsorption equilibrium studies at 25, 35 and 45°C, the thermodynamic parameters were determined. Two different regeneration methods were employed in order to test the reusability of the adsorbent.

MATERIALS AND METHODS

Materials

Commercial synthetic zeolite 13X (Sigma-Aldrich, 3.2 mm pellets, Si/Al=1.2) was used as the adsorbent in the present study. The extrudates were ground in a mortar and sieved to particle diameter of 75–150 μm. Prior to the adsorption of acetic acid, these particles were activated in a static oven at 320 °C for 24 hours.

Experimental procedure

The stock solution of acetic acid (Carlo Erba, glacial, %99.5–100.5) was prepared by using distilled water. The solutions which were used in the adsorption kinetic and equilibrium experiments with the initial acetic acid concentrations in the range of 0.03–0.54 mol/L (0.17–3.25 wt. %) were prepared by diluting the stock solution. Two grams of 13X were contacted with 100 mL of acetic acid solutions of different initial concentrations in a thermostatic water bath at 25, 35 and 45°C at a shaking speed of 150 rpm. The samples which were taken from the supernatant at specific times were titrated with 0.05 M aqueous NaOH solution in order to determine the acetic acid concentration in the solution. The amount of acetic acid adsorbed was calculated as follows:

$$q_t = \frac{(C_o - C_t)V}{m} \qquad \text{(Eq. 1)}$$

where q_t is the amount of acetic acid adsorbed at the specified time, C_o is the initial acetic acid concentration of the solution, C_t is the acetic acid concentration in the solution at the specified time, V is the volume of the solution, and m is the adsorbent mass.

Regeneration of the adsorbent is a critical step as it influences the overall economy of the process. In order to test regenerability of the adsorbent, the 13X particles were saturated with acetic acid, then washed with distilled water and dried in a static oven at 60 °C overnight. One gram of these particles was then contacted with 50 mL of distilled water in the thermostatic water bath at 45 °C. The samples which were taken at specific time intervals were titrated with a NaOH solution in order to determine the amount of acetic acid desorbed. As another regeneration method, the acetic acid-saturated 13X particles were kept in a static oven at 300 °C for 24 hours and were used in acetic acid adsorption at 25 °C again.

Adsorption Kinetics

During adsorption of acetic acid molecules in 13X, the acid molecules were first transferred from the bulk solution to the external film surrounding the adsorbent particle (through the interparticle pores), then through the external film and through the intraparticle pores. Then sorption occured

at the adsorption sites by chemisorption or ion exchange or physisorption. The rate of sorption might be controlled by the slowest mass transfer step.

In order to investigate the mechanism of adsorption of acetic acid in the 13X particles, the pseudo-first-order (71), pseudo-second-order (72) and intraparticle diffusion (73) models were employed. The model equations are given in Table 1.

Table 1: Adsorption kinetic models employed to the experimental kinetic data for acetic acid adsorption in 13X.

Model	**Equation**	**Eqn. number**
Pseudo first-order	$\log(q_e - q_t) = \log q_e - \frac{k_1}{2.303} t$	(Eq. 2)
Pseudo second-order	$\frac{t}{q_t} = \frac{1}{k_2 q_e^2} + \frac{1}{q_e} t$	(Eq. 3)
Intraparticle diffusion	$q_t = k_i \sqrt{t} + c$	(Eq. 4)

In these equations q_t and q_e are the amounts of acetic acid adsorbed at time t and equilibrium, respectively, k_1 is the pseudo-first-order rate constant for the adsorption process, k_2 is the pseudo-second-order rate constant for the adsorption process, k_i is the intraparticle diffusion constant, and c is the thickness of the boundary layer formed between the adsorbate molecules and the adsorbent surface.

The goodness of fit was evaluated based on the linearity of the $\log(q_e\text{-}q_t)$ versus t, t/q_t versus t and q_t versus $t^{0.5}$ plots for the pseudo first-order, pseudo second-order and intraparticle diffusion models, respectively.

Adsorption Equilibrium

Adsorption equilibrium isotherm describes how the adsorbate molecules distribute between the liquid and the solid phases at equilibrium.

Two-parameter (Langmuir, Freundlich, Temkin, Dubinin–Radushkevich models), and three-parameter (Redlich–Peterson, Toth, Sips models) adsorption equilibrium models were employed to describe the acetic acid adsorption kinetics in 13X in the present study. The model equations are given in Table 2.

Table 2: Adsorption equilibrium models

Model	**Equation**	**Eq. no.**
Langmuir	$q_e = \frac{q_m K_L C_e}{1 + K_L C_e}$	(Eq. 5)
Freundlich	$q_e = K_F C_e^{1/n_F}$	(Eq. 6)
Temkin	$q_e = \frac{RT}{b} \ln(K_T C_e)$	(Eq. 7)
Dubinin-Radushkevich (D-R)	$q_e = q_{mDR} \exp(-K_{DR} \varepsilon^2)$	(Eq. 8)
Redlich-Peterson (R-P)	$q_e = \frac{K_{RP} C_e}{1 + a_{RP} C_e^g}$	(Eq. 9)
Sips (Langmuir–Freundlich)	$q_e = \frac{q_m (a_s C_e)^{1/n_s}}{1 + (a_s C_e)^{1/n_s}}$	(Eq. 101)
Toth	$q_e = \left[\frac{q_m a_T C_e}{1 + (a_T C_e)^{n_T}}\right]^{1/n_T}$	(Eq. 11)

In these equations, C_e is the concentration of acetic acid in solution at equilibrium, q_m is the saturation adsorption capacity, q_{mDR} is the D–R model constant related to the degree of adsorption by the adsorbent under the optimized experimental conditions, K_L is the Langmuir model adsorption equilibrium constant related to the adsorption energy, K_F is the Freundlich model constant related to the adsorption capacity, n_F is the Freundlich model constant related to the adsorption intensity, b is the Temkin model constant related to heat of adsorption, K_T is the Temkin model equilibrium binding constant corresponding to the maximum binding energy, K_{DR} is the Dubinin-Radushkevich model adsorption equilibrium constant related to the adsorption energy, ε is the Polanyi potential, K_{RP} is the Redlich-Peterson model adsorption equilibrium constant, a_{RP} is the Redlich-Peterson model affinity consant, g is the Redlich-Peterson model exponent (Redlich-Peterson model reduces to the Langmuir isotherm for g=1), a_s is the Sips model affinity consant, n_s is the Sips model parameter characterizing the system heterogeneity, a_T is the Toth model affinity consant, n_T is the Toth model parameter characterizing the system heterogeneity, R is the gas constant, and T is the absolute temperature.

The equations for the adsorption equilibrium models given in Table 2 were fitted to the experimental data using the Generalized Reduced Gradient (GRG) nonlinear regression algorithm of Excel Solver. The model parameters minimizing the sum of the squares of the errors (*SSE*) were calculated. The *SSE* values for the model fittings were calculated as follows:

$$SSE = \sum \left(q_{e,model} - q_{e,exp}\right)^2 \qquad \text{(Eq. 12)}$$

where $q_{e,model}$ and $q_{e,exp}$ are the calculated and experimentally measured adsorbate concentrations at equilibrium, respectively.

Fourier Transform Infrared Spectroscopy (FTIR)

The 13X zeolite was characterized before and after activation, acetic acid adsorption, regeneration in deionized water at 45 °C and heating at 300 °C successive to the saturation with acetic acid by used transmittance FTIR spectroscopy. The samples were prepared using the standard KBr pellet method (sample/KBr weight ratio of 1/200). The sample-KBr mixtures were ground together in an agate mortar and pelletized under 10 tons pressure by a hydraulic press. The spectra were recorded in the region of 400–4000 cm^{-1} at room temperature after 128 scans at 2 cm^{-1} resolution using a spectrometer (Spectrum II, Perkin Elmer). For all the spectra, the baseline correction was performed.

RESULTS and DISCUSSION

Adsorption Kinetics

From the experimental adsorption kinetics data shown in Figure 1, it was concluded that the equilibrium has been reached within the first 240 minutes. The acetic acid removal efficiency (%) is calculated by following equation:

$$\%\text{removal efficiency} = \frac{C_o - C_e}{C_o} \times 100 \quad \text{(Eq. 13)}$$

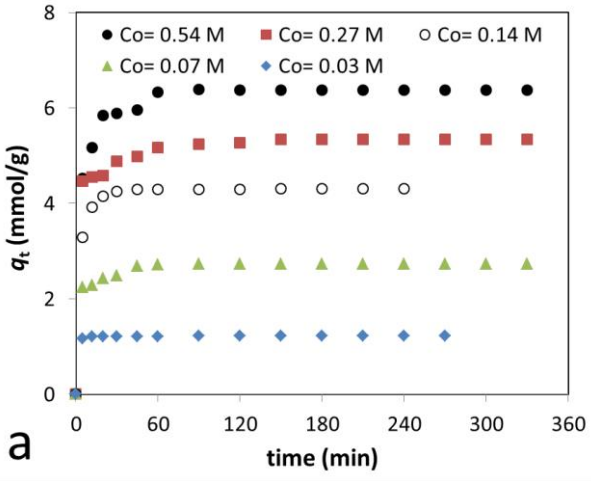

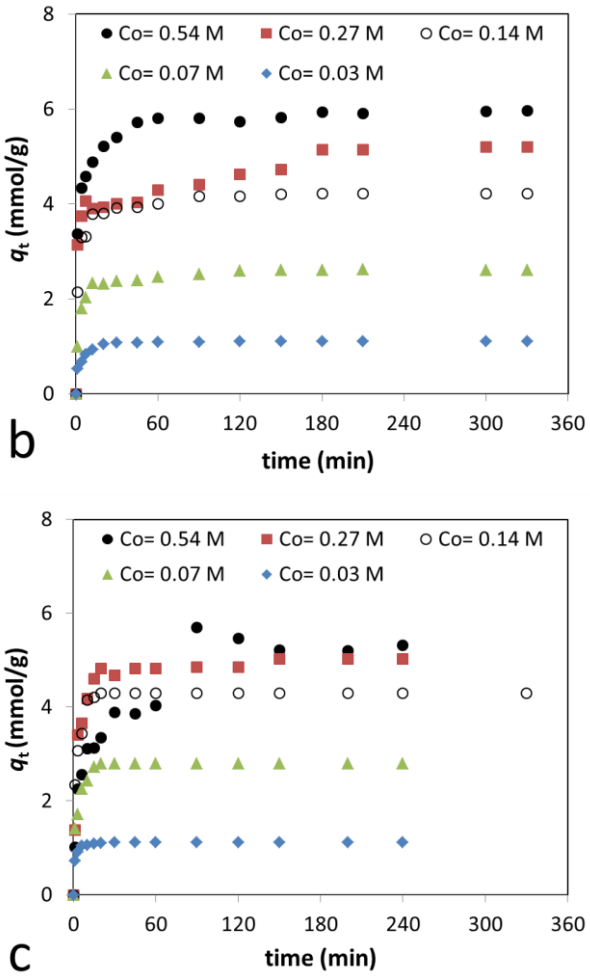

Figure 1: Variation of the amount of acetic acid adsorbed in 13X with time for different initial acetic acid concentratons at (a) 25°C, (b) 35°C and (c) 45°C.

The acetic acid removal efficiency of the 13X zeolite decreased with the initial acetic acid concentrations but was not affected remarkably by the adsorption temperature as seen in Figure 2.

The values of the kinetic parameters (q_e, k_1, k_2, k_i, and c) and the regression coefficients (r^2) were determined from the intercepts and slopes of the linear plots using the corresponding kinetic model equations in Table 1.

The regression coefficients (r^2) calculated form the pseudo-first and pseudo-second order models are given in Table 3. The correlation coefficients calculated for the pseudo-second order kinetic model fitting are significantly higher than those obtained for the pseudo-first order kinetic model for the whole acetic acid concentrations and temperatures indicating that the experimental adsorption kinetic data can be represented by the pseudo-second-order kinetic model. This revealed that the adsorption rate is controlled by a chemical reaction between the 13X surface and acetic acid molecules involving valency forces through sharing or exchange of electrons between sorbent and sorbate (72).

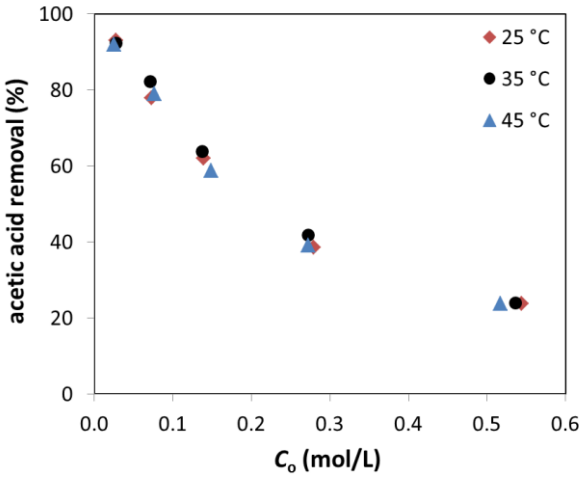

Figure 2: Variation of the acetic acid removal efficiency with the initial acetic acid concentration at 25, 35 and 45°C.

Table 3: Comparison of the regression coefficients for linearized pseudo-first and pseudo-second order kinetic models at various initial concentrations and temperatures.

C_o (mol/L)	25°C		35°C		45°C	
	Pseudo-first order	Pseudo-second order	Pseudo-first order	Pseudo-second order	Pseudo-first order	Pseudo-second order
0.54	0.875	1.000	0.830	1.000	0.754	0.993
0.27	0.826	1.000	0.904	0.997	0.552	1.000
0.14	0.954	1.000	0.885	0.999	0.956	1.000
0.07	0.920	1.000	0.908	0.999	0.967	0.999
0.03	0.507	1.000	0.878	1.000	0.925	1.000

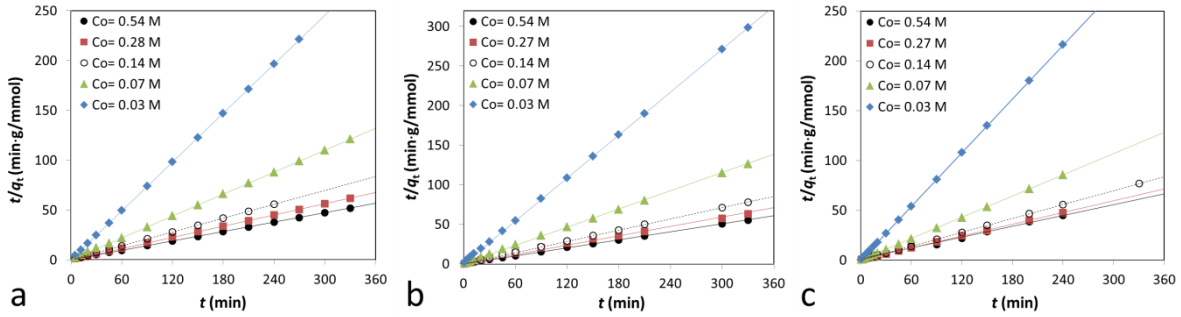

Figure 3: t/q_t versus t plots for adsorption at (a) 25°C, (b) 35°C and (c) 45°C.

The values q_e and k_2 calculated from the linear plots of t/q_t versus t shown in Figure 3 are presented in Table 4. The calculated q_e values obtained from this model were in excellent agreement with the experimental ones. The model represented the experimental data fairly well in the whole concentration and temperature range of interest in the present study.

The pseudo-second order kinetic rate constant (k_2) values were found to decrease while the equilibrium adsorption capacities (q_e) increased with the increasing initial acetic acid concentration. The equilibrium sorption capacity (q_e) did not change significantly with the

temperature at the low initial acetic acid concentrations while it decreased with the increasing temperature at the higher initial acetic acid concentrations. This suggested that the acetic acid adsorption in 13X zeolite is favored at low temperatures and high initial acetic acid concentrations.

Table 4: Pseudo second-order model parameters.

T (°C)	C_o (mol/L)	k_2 (g/mmol·min)	q_e (mmol/g)
25	0.54	0.079	6.42
	0.28	0.073	5.39
	0.14	0.259	4.33
	0.07	0.235	2.74
	0.03	3.281	1.22
35	0.54	0.066	5.99
	0.27	0.023	5.27
	0.14	0.112	4.25
	0.07	0.145	2.63
	0.03	0.577	1.11
45	0.52	0.019	5.54
	0.27	0.087	5.06
	0.15	0.479	4.30
	0.08	0.430	2.81
	0.03	2.783	1.11

From the q_t versus $t^{0.5}$ plots drawn according to the intraparticle diffusion model (for 35°C shown in Figure 4), it was found that all the plots exhibited three linear regions involved in adsorption of acetic acid in 13X zeolite. The initial linear region where the adsorbed amount of acetic acid increased rapidly corresponds to the adsorption on the external surface of the 13X particles. The linear regions at later times where the adsorption occurs at a gradual rate represent adsorption of the adsorbate molecules in the adsorbent particles (in mesopores between the zeolite crystals and within the crystals) (73).

None of these plots passed through the origin (c is not equal to zero) implying that the intraparticle diffusion was not the only rate-controlling step in the adsorption of acetic acid in 13X (73). The k_i and c values calculated respectively from the slopes and intercepts of the linear portions together with the regression coefficients (r^2) for adsorption at 35°C are given in Table 5. The k_i values (rate of adsorption) at the later period of the adsorption were lower than those at the beginning of the adsorption due to decrease in the mass transfer rate due to the low acetic acid concentration left in the solution, i.e. lower driving force. The values of c decreased with the decreasing initial acetic acid concentration.

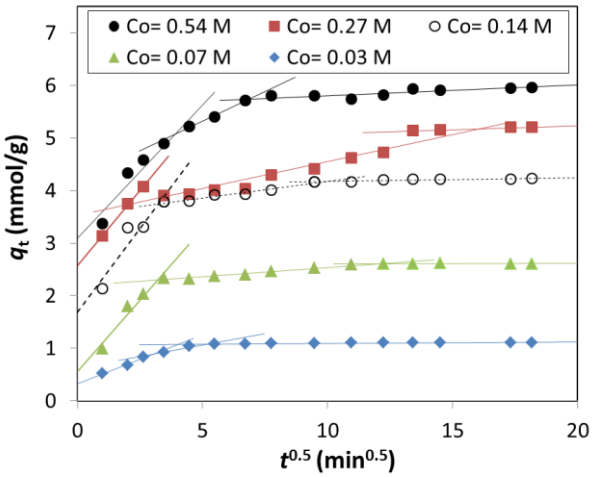

Figure 4: q_t versus $t^{0.5}$ plots for the acetic acid adsorption at 35 °C.

Table 5: Intraparticle diffusion control model parameters for the acetic acid adsorption at 35°C.

C_o (mol/L)	r^2	k_i (mmol/g·min$^{0.5}$)	c
		1st linear region	
0.54	0.911	0.373	3.414
0.27	0.997	0.573	2.570
0.14	0.892	0.635	1.684
0.07	0.952	0.541	0.554
0.03	0.978	0.185	0.329
		2nd linear region	
0.54	0.992	0.225	4.192
0.27	0.878	0.102	3.530
0.14	0.957	0.062	3.546
0.07	0.971	0.035	2.182
0.03	0.949	0.088	0.618
		3rd linear region	
0.54	0.771	0.020	5.600
0.27	0.989	0.015	4.937
0.14	0.767	0.007	4.106
0.07	0.109	0.001	2.602
0.03	0.650	0.003	1.057

Adsorption Equilibrium

The values of the model parameters and *SSE* for the adsorption equilibrium models are given in Table 6. Considering these *SSE* values given in Table 6, it is evident that the experimental equilibrium data can be represented better by the three-parameter models (R-P, Sips and Toth models) than by the two-parameter models (Langmuir, Freundlich, Temkin and D-R models). The *SSE* values for the Sips model were the lowest among those for the equilibrium models

fitted. Thus it was concluded that the experimental adsorption equilibrium data can be represented best with the Sips model.

Table 6: Adsorption equilibrium model parametres and *SSE* values for the fitted equilibrium models.

Model	**Parameter**	**25°C**	**35°C**	**45°C**
Langmuir	q_m	6.319	5.916	5.402
	K_L	47.316	61.926	73.708
	SSE	0.750	0.343	0.217
Freundlich	K_F	8.30	7.89	7.15
	n_F	3.82	3.99	4.33
	SSE	0.43	0.77	0.93
Temkin	*b*	2.567	2.723	3.157
	K_T	1533.3	1520.1	1999.5
	SSE	0.201	0.071	0.179
Dubinin-Radushkevich	q_{mDR}	6.265		
	K_{DR}	0.0069		
	SSE	0.334	0.031	0.291
Redlich-Peterson	K_{RP}	1154.7	702.6	654.6
	a_{RP}	150.6	102.7	108.8
	g	0.811	0.876	0.912
	SSE	0.106	0.042	0.093
Sips	q_m	8.68	6.92	5.97
	a_s	15.91	37.98	56.93
	n_s	1.90	1.53	1.41
	SSE	0.061	0.012	0.022
Toth	q_m	11.112	7.485	6.222
	a_T	507.0	186.3	175.1
	n_T	0.311	0.491	0.580
	SSE	0.068	0.015	0.038

Fitting of the Sips model to the experimental adsorption isotherms at 25, 35 and 45°C are shown in Figure 5. It can also be seen that the amount of acetic acid adsorbed at equilibrium decreased with the increasing adsorption temperature.

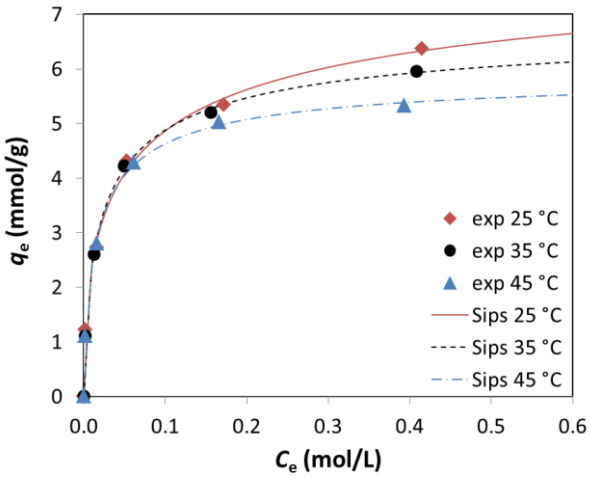

Figure 5: Experimental adsorption equilibrium data and the Sips model fittings.

The Sips model parameter characterizing the system's heterogeneity (74) was found to decrease with the increasing temperature suggesting that the system is "apparently" less heterogeneous at higher temperatures. However, this does not point to what is the source of the heterogeneity, whether it is the adsorbent structural property, the adsorbent energetical property or the sorbate property (74).

The temperature dependence of the Sips model adsorption affinity constant (a_s) has the following form (74):

$$a_s = a_{s\infty} \exp(Q/RT) \qquad \text{(Eq. 14)}$$

where $a_{s\infty}$ is the affinity constant at infinite temperature and Q is the adsorption heat.

From the linear plot of lna_s versus $1/T$ (Figure 6) (r^2=0.965), the adsorption heat (Q) and $a_{s\infty}$were calculated as 50.40 kJ/mol and 1.16×10^{10} L/mol, respectively. The calculated Q corresponds to the isosteric heat at the fractional loading of 0.5 (74).

Zhang and co-workers stated that the experimental acetic acid adsorption isotherms for 13X pellets (Si/Al<3) can be represented by the Freundlich model and determined the model parameters as K_F=1.20 mmol/g and n_F=2.66 at 25°C. The amount of acetic acid adsorbed increased with the initial acetic acid concentration and temperature (endothermic adsorption). The monolayer acetic acid adsorption capacity of was calculated as 6.38, 6.75 and 7.11 mmol/g at 25, 35 and 45°C, respectively, by the Langmuir model (60). The same research group had found that the adsorbed amount of acetic acid decreased with increasing temperature, indicating that acetic acid adsorption on UiO-66 was exothermic. The monolayer acetic acid adsorption capacity of the MOF was calculated as 4.50 and 4.73 at 25 and 45°C, respectively (61). The monolayer acetic acid adsorption capacity of 13X used in the present study at 25°C (6.32

mmol/g) was shown to be in good agreement with that reported for the 13X pellets (Si/Al<3) (6.38 mmol/g) (60), and higher than those of 330 resin (0.53 mmol/g) (75), activated carbon (0.92 mmol/g) (48), multiwall carbon nanotube (0.09 mmol/g) (56) and UiO-66 (4.50 mmol/g) (61).

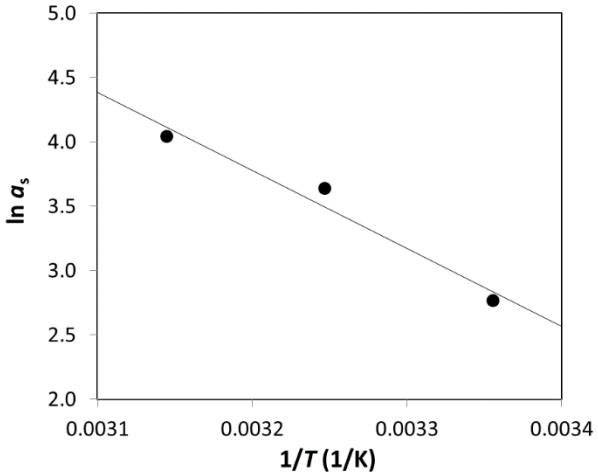

Figure 6: Temperature dependence of the Sips model parameter a_s.

Langmuir model constant, K_L, indicates the affinity for the binding of acetic acid. A dimensionless constant, commonly known as dimensionless separation factor (R_L) can be represented as (76):

$$R_L = \frac{1}{1+K_L C_o} \quad \text{(Eq. 15)}$$

The R_L value indicates whether the adsorption is unfavorable (R_L>1), linear (R_L=1), favorable (0<R_L<1) or irreversible (R_L=0) (77). In the present study, the R_L values were found to vary within the range of 0.026–0.434 indicating the favorable adsorption. The R_L values decreased as the temperature and initial acetic acid concentration increased (Figure 7).

Although it was found in the present study that the experimental adsorption equilibrium data can be represented by the Sips model better, the monolayer adsorption capacity (q_m) calculated from the Langmuir model fitting was used to calculate the specific surface area (S) of the 13X as follows:

$$S = A_a N_A q_m \quad \text{(Eq. 16)}$$

where N_A is Avogadro's number and A_a is the cross-sectional area of the adsorbate molecule. Assuming that the acid molecules are adsorbed vertically, with the alipatic chain up and the carboxyl group down attached to the adsorbent surface, the cross-sectional area of a straight-chain acid was taken to be about 21×10^{-20} m^2 (78). From the monolayer adsorption capacities

were calculated from the Langmuir model fitting, the average specific surface area of the 13X was calculated as 745 m^2/g. This value fell in the range of the reported BET surface areas (500–800 m^2/g) measured with N_2 adsorption data at -196 °C for X and Y type zeolites (79).

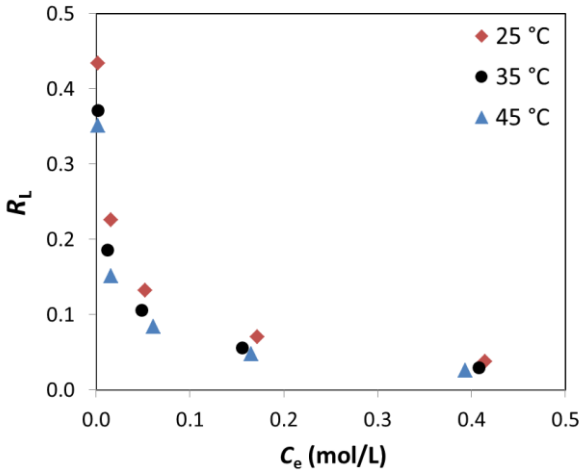

Figure 7: Separation factor as a function of the initial acetic acid concentration and temperature.

The Dubinin–Radushkevich (D-R) model, given in Table 2 by Eqn.(8), is a semi-empirical model which is originally developed for sub-critical vapors in microporous solids, where the adsorption process follows a pore filling mechanism onto an energetically non-uniform surface (80). D–R model is rarely applied to liquid-phase adsorption due to the complexities associated with other factors such as pH and ionic equilibria inherent in these systems. Additionally, the solute-solvent interactions often render the bulk solution non-ideal. However the model was applied to adsorption from liquid phase using 13X zeolite in the literature (81-84). In this model the Polanyi potential (ε) is expressed by the equation below;

$$\varepsilon = RT\ln\left(1+\frac{1}{C_e}\right) \qquad \text{(Eq. 17)}$$

The experimental data and the D-R model fittings plotted using the model parameters given in Table 6 were shown in Figure 8. Even though only one value of the characteristic energy was used in the fitting of the experimental data at three temperatures, the fit is very good (r^2=0.993) demonstrating the effectiveness of this model in describing the experimental data for acetic acid adsorption in 13X.

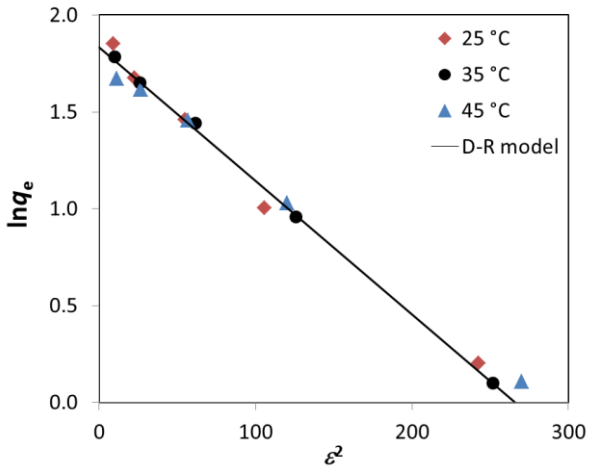

Figure 8: Experimental characteristic curve and the D-R model fitting.

The D-R model adsorption equilibrium constant K_{DR} is related to the mean free energy of transfer of one mole of solute from infinity in solution to the adsorbent surface as:

$$E = \frac{1}{\sqrt{2K_{DR}}} \qquad \text{(Eq. 2)}$$

This parameter gives information about the adsorption mechanism: If the magnitude of E is between 8 and 16 kJ/mol the adsorption process follows by ion exchange, while the value below 8 kJ/mol the adsorption process is of a physical nature (85). In the present study the calculated value of E (8.51 kJ/mol) is slightly above 8 kJ/mol suggesting that the removal of acetic acid by 13X occurred by both physisorption and ion exchange mechanisms.

The micropore volume of 13X pellets was calculated as 0.359 cm^3/g using the saturation adsorption capacity corresponding to the D-R maximum pore volume (calculated from q_{mDR}). This value is in good agreement with the pore volume of NaX (Si/Al=1.25) determined from the adsorption of different types of molecules including water, gases and hydrocarbon (0.25–0.36 cm^3/g) in the literature (86).

Adsorption Thermodynamics

The change in the standard Gibbs free energy of adsorption (ΔG°) can be expressed as:

$$\Delta G^\circ = -RT\ln K = -RT\ln(55.5K') \qquad \text{(Eq. 3)}$$

where K is the dimensionless equilibrium constant and 55.5 is the activity of water in solution. K' was determined from C_e versus C_e/q_e plots. Temperature dependence of the dimensionless adsorption equilibrium constant is given by the van't Hoff equation,

$$\ln K = \frac{\Delta S^o}{R} - \frac{\Delta H^o}{RT} \qquad \text{(Eq. 4)}$$

where ΔH° is the standard enthalpy of adsorption and ΔS° is the standard entropy of adsorption. The values of ΔH° and ΔS° were calculated from the slope and intercept of the van't Hoff plot shown in Figure 9, respectively. The values of ΔG°, ΔH° and ΔS° are given in Table 7.

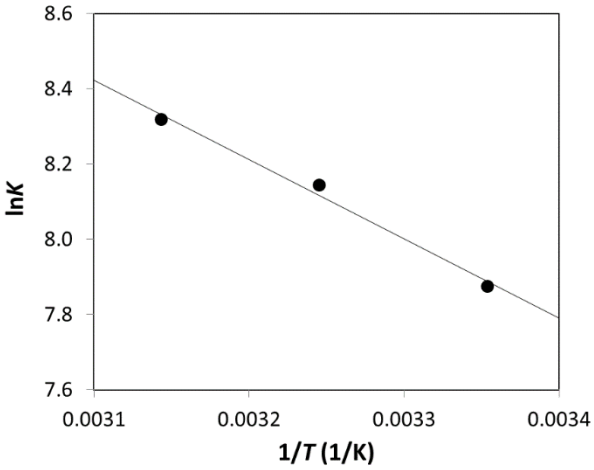

Figure 9: van't Hoff plot(ln *K* versus 1/*T*)

Table 7: Thermodynamic parameters.

***T* (°C)**	**Δ*G*° (kJ/mol)**	**Δ*H*° (kJ/mol)**	**Δ*S*° (J/mol/K)**
25	-19.52		
35	-20.86		
45	-22.00		

The negative ΔG° values indicated spontaneous adsorption of acetic acid on 13X zeolite. The values of $\Delta G°$ decreased from -19.52 to -22.00 kJ/mol with increase in temperature from 25°C to 45 °C indicating that the sorption of acetic acid was favorable at high temperatures. The positive $\Delta H°$ values designated that the sorption of acetic acid in 13X was endothermic. However, as previously stated and shown in Figure 5, the amount of acetic acid adsorbed at equilibrium decreased with the increasing temperature. The reason for this is that in the low acetic acid concentration range in which the dimensionless adsorption equilibrium constant (*K'*) was calculated the amount of acetic acid adsorbed at equilibrium increased with temperature. This indicates that the interaction between the acetic acid molecules and the 13X surface increased with temperature in the low acetic acid concentration range, while weaker interaction between the acetic acid and adsorbent than that between water and the adsorbent at high acetic acid concentration range (87). The positive values of entropy change ($\Delta S°$) implied the increased randomness (degree of freedom of the system) at the solid-solute interface during adsorption, which may be caused by the restricted mobility of acetic acid on the surface of 13X particles compared with that of aqueous solution (88).

Regeneration of the Adsorbent

In order to determine the reusability of the 13X adsorbent, a consecutive adsorption–desorption cycle was conducted. In the present study the 13X zeolite saturated with acetic acid (88) was regenerated using two different methods: shaking with distilled water at 45 °C (1 g of solid/100 mL of water) and heating to 300 °C under static aereal atmosphere. The acetic acid-saturated 13X did not desorb the acetic acid in distilled water at 45 °C as seen in Figure 10. From Figure 11, it can be seen that the acetic acid adsorption capacity of the 13X particles at 25 °C after being regenerated at 300 °C has dropped to about half of that of the fresh 13X.

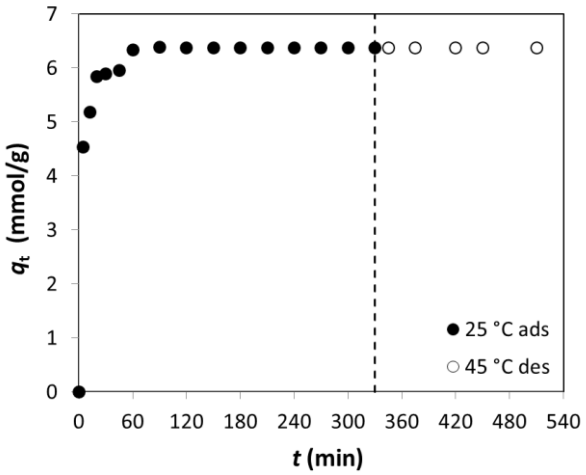

Figure 10: Desorption kinetics of acetic acid at 45°C in distilled water after the acetic acid adsorption at 25°C.

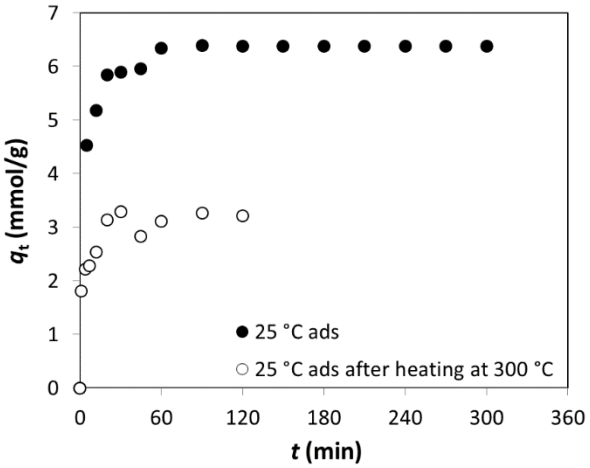

Figure 11: Acetic acid adsorption kinetics for the fresh and heated (at 300°C) 13X after being saturated with acetic acid.

For regeneration of the acetic acid loaded activated carbons and macroreticular styrene-divinylbenzene adsorbents, methanol, methyl acetate, and acetone were suggested as suitable regeneration solvents (49). Lv and co-workers regenerated acetic acid-loaded ion exchange resin with 2 to 4 % NaOH solution efficiently without harming the resin (75). In another study, a

metal-organic framework (UiO-66) was washed with deionized water and ethanol, and reused in acetic acid adsorption. After three adsorption-desorption cycles, the adsorption capacity of UiO-66 decreased by 7% without any deformation in the structure of UiO-66 (61). Ethanol was suggested as an adsorption-competitive solvent for the regeneration of the high-silica ZSM-5 powder (58). In fixed-bed separation process by concentration swing adsorption where activated carbon was used as the adsorbent the bed was rinsed with acetone to displace acetic acid and water from the bed (15). However, these regeneration processes increase the operational cost and cause environmental pollution as they require use of chemicals. Acetic acid decomposes to form CO_2 and methane or to form ketene and water above 440 °C (89, 90). However this temperature may harm the adsorbent concerning the regeneration temperature given by the producer (91).

Fourier Transform Infrared Spectroscopy (FTIR)

The strongest band in the spectrum of 13X was detected at 966 cm^{-1} with a shoulder at 1072 cm^{-1}. These bands are due to the asymmetric T–O stretching vibrations (T: tetrahedral Si or Al atoms). The band at 467 cm^{-1} corresponds to the O–T–O angular deformation (T–O bending) vibrations. The bands at 697 and 746 cm^{-1} are due to symmetric O–T–O stretching vibrations and are attributed to internal tetrahedral stretch and external linkage symmetric stretch, respectively. 568 cm^{-1} band corresponds to the vibrations of the double rings (D6R rings). The bands at 966, 697 and 467 cm^{-1} are due to internal vibrations of the TO_4 tetrahedron which is the primary unit of structure and which are not sensitive to structural variations. The bands at 1072, 746 and 568 cm^{-1} are sensitive to the linkages between tetrahedra (external linkages) and the topology and mode of arrangement of the secondary units of structure. The band at 1656 cm^{-1} is due to the angular deformation of H–O–H bonds (H–O–H bending mode of water molecule) (86).

No significant changes neither in frequency nor in absorbance of the bands in the 400–1200 cm^{-1} region was observed after the activation of 13X at 320 °C (Figure 12A, spectrum b). The changes in bands in the the O–H stretching region are discussed below.

Upon adsorption of acetic acid from the solution with the initial acid concentration of 0.54 M at 25 °C resulted in a shift of the 966 cm^{-1} band to 1059 cm^{-1} and 1072 cm^{-1} band to 1156 cm^{-1} (Figure 12A, spectrum c). The frequency of 966 cm^{-1} band varies linearly with the number of aluminum atoms in the framework tetrahedral sites (86). Thus the shift of 966 cm^{-1} band to a higher frequency after the acetic acid adsorption indicated a decrease in the number of aluminum atoms in the framework tetrahedral sites. Dealumination of zeolites is partially due to action of proton. In acidic to neutral solutions, the protons in the solution can be adsorbed to the neutral and negative surface groups and thereby protonate them (proton binding). The formation of the

≡Al-OH_2^+ surface complexes increases aluminum dissolution and consequently increases Al^{3+} hydrolysis (92).

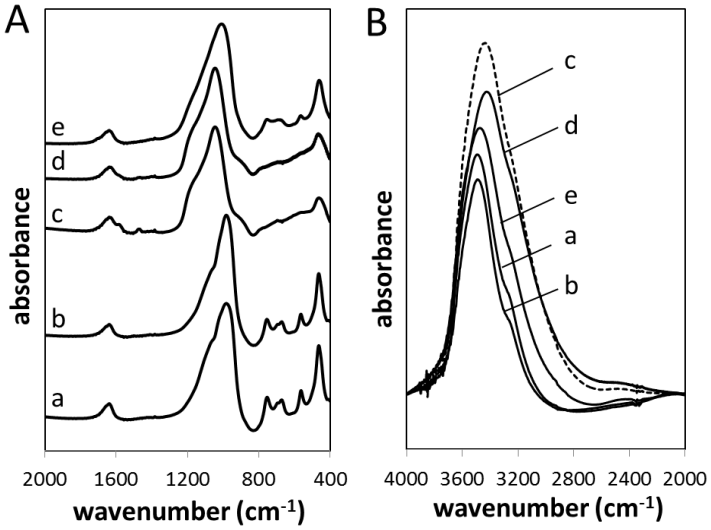

Figure 12: Absorbance IR spectra of 13X (A) 400–2000 cm^{-1} region and (B) 2000–4000 cm^{-1} region. (a) before activation, (b) after activation, (c) after acetic acid adsorption at 25°C (C_o=0.54 M), (d) after desorption in deionized water at 45°C and (e) after heating at 300°C subsequent to the adsorption.

Upon acetic acid adsorption, the bands at 467 cm^{-1} and 697 cm^{-1} lost intensity and the bands at 568 and 746 cm^{-1} disappeared. As mentioned above, the bands at 997, 697 and 467 cm^{-1} are due to internal vibrations of the primary building units (TO_4 tetrahedra) and are not sensitive to structural variations while the bands at 746 and 568 cm^{-1} are sensitive to the linkages between tetrahedra (external linkages). Thus it may be concluded that aluminum removal from the framework sites upon acid adsorption led to changes in the external vibrations (secondary structure, linkages between the tetrahedral units) but did not change the internal tetrahedral vibrations significantly. The perturbations observed can be associated to T–O bond length, T–O–T and O–T–O angles (93, 94). The disappearance of the band at 568 cm^{-1} suggested that the external linkages were broken as a result of aluminum removal, *i.e.* that aluminum removal left "holes" in the framework. Moreover, the formation of holes or the replacement of Al atoms by H atoms involves changes in the frequencies and new bands or shoulders probably occur (95). These perturbations created a new shoulder band at 900 cm^{-1}.

Adsorption of acetic acid on 13X led to appearance of new bands in at 1390, 1472 and 1593 cm^{-1}. The intensities of these bands were low since the acetic acid adsorption was performed in a dilute acidic solution with low sorbent/solution ratio (2 g of sorbent/100 mL of solution). The bands in the region of 1550–1610 cm^{-1} and 1300–1420 cm^{-1} were assigned to carboxylate (carboxylic acid salt) while those in the 1700–1725 cm^{-1} region to carboxylic acid (96). The weak band at 1390 cm^{-1} can be attributed to asymmetric deformation vibration of CH_3. The band at

1472 cm^{-1} and the shoulder at 1593 cm^{-1} may be assigned to the symmetric C–O stretching and asymmetric stretching vibrations of the COO^- group, respectively (97, 98).

Regeneration of the acetic acid-saturated 13X in deionized water at 45°C was led to loss in intensities of the bands at 1390, 1472 and 1593 cm^{-1} (Figure 12A, spectrum d) indicating dissolution of the weakly adsorbed species were associated with these bands. Any significant change was observed in the intensity or frequency of the bands in the 400–1400 cm^{-1} spectral region.

In the spectra which were taken after heating at 300 °C (Figure 12A, spectrum e), the intensities of the 467 and 697 cm^{-1} bands increased almost to their values in the spectrum for activated 13X and the bands at 568 and 746 cm^{-1} reappeared in the spectrum. The main asymmetric stretching band at 1059 cm^{-1} was hifted back to 994 cm^{-1} and the asymmetric stretching band (detected as a shoulder in the spectrum of 13X at 1072 cm^{-1}) disappeared. These indicated the reconstruction of the secondary building units. The bands at 1472 and 1593 cm^{-1} were disappeared whereas 1390 cm^{-1} band was remained and a very weak shoulder band was appeared at 1720 cm^{-1}. In the literature the band at 1720 cm^{-1} was detected in the spectrum of acetic acid dissolved in CCl_4 and assigned to the stretching vibrations of the C=O group (97, 99).

Evacuation of acetic acid vapor adsorbed NaHY at 200 °C led to a decrease in the intensity of the typical bands of acetic acid (1690 and 1280 cm^{-1}) and appearance of a doublet at 1580-1610 cm^{-1} and a band at 1480 cm^{-1}. These new bands were similar to those in the spectrum of sodium acetate. Evacuation at 300 °C resulted in a diminishing of the bands of unreacted acetic acid molecules, without any decrease of the intensity of acetate ion bands. This suggested that acetate ions formed in NaHY were stable until 300 °C (99).

O-H stretching region

In the O–H stretching region, a broad band in the 3000–3800 cm^{-1} region with maximum at 3506 cm^{-1} and with a shoulder at 3288 cm^{-1} were detected in the spectra of 13X before activation (Figure 12B, spectrum a). The intensities of 3506 and 3288 cm^{-1} bands decreased slightly after the activation (Figure 12B, spectrum b). However after the activation since 13X was exposed to atmosphere during the preparation of the KBr pellets thereby adsorbed water vapor, it was not possible to resolve the peaks in the O–H stretching region due to presence of water clusters giving the broad band superimposing the O–H bands if present.

The bands in this region are attributed to the O–H bond stretching of the surface hydroxyl groups or O–H stretching mode of the water molecules (100). Surface hydroxyl groups in zeolites originate from several sources: Acidic O–H groups due to framework Al and other trivalent ions such as B, Ga, Fe, etc.; silanol groups (Si–OH) on the external surface and in the "nests" (defect

sites); O–H groups attached to di- or tri-valent cations due to hydrolysis; O–H groups from "dangling Al"; O–H groups associated with non-framework aluminum species and O–H groups of adsorbed water. The O–H groups attached on the charge balancing ions formed via hydrolysis can also be observed (101). The theoretical structure of X-type zeolite does not include any O–H groups. However cation deficient form of NaX may exhibit properties associated with hydroxyl groups due to partial hydrolysis of the Na^+ cations and replacement by hydronium ions (86).

For the activated NaX, presence of various bands in the 3000-3800 cm^{-1} range of the spectra was explained by the presence of several types of hydroxyl groups. The band at 3645 cm^{-1} was assigned to free acidic O–H groups bridging Al and Si atoms, pointing towards the supercages (102, 103), while other types of acidic hydroxyls gave bands in the 3200-3600 cm^{-1} range (103). These bands were related to cation deficiencies of NaX due to the fact that exchangeable cations (*e.g.* Na^+) were partially hydrolyzed during the preparation or the subsequent washing treatment (104).

However in order to resolve the various O–H groups, the adsorbed water must be removed so the sample must be activated *in situ*. In the present study NaX was in fully hydrated state since the acetic acid adsorption was studied in the aqueous solutions.

Zeolites always adsorb water when they are exposed to the atmosphere due to their hydrophilic properties. The adsorbed water in zeolites can be present in the forms of free water, loosely coordinated water, tightly coordinated water and even water clusters (105). Infrared spectroscopic studies of water adsorption in faujasites revealed the existence of different structures of adsorption complexes depending on the water loading (106-110). The water-bending vibration at 1640 cm^{-1} indicates the presence of adsorbed water in zeolites. Due to the hydrogen bonding of water with O–H groups, the bands in the hydroxyl spectral region (3000–4000 cm^{-1}) are generally structureless and broad (101). Beta and co-workers reported a broad band at about 3400–3500 cm^{-1} with a shoulder at about 3180–3250 cm^{-1} in the diffuse reflectance infrared Fourier transform (DRIFT) spectra of the hydrated faujasites (including NaX). The latter was assigned to the collective in-phase O–H stretching vibrations of hydrogen bonded aggregates consisting of a central water molecule and its nearest and higher neighbors. The band at about 3400–3500 cm^{-1} was assigned to O-H stretchings of water molecules which are hydrogen bonded to framework oxygen (107).

The intensity and width of the 3506 cm^{-1} band increased remarkably after the acetic acid adsorption (Figure 12B, spectrum c). Intensity of this band decreased after the rinsing in water without change in the width (Figure 12B, spectrum d). The intensity further declined and the band has become less broadened upon heating at 300 °C (Figure 12B, spectrum e). The band at 3506 cm^{-1} shifted to 3458 cm^{-1} after the acetic acid adsorption, to 3446 cm^{-1} after rinsing at

45 °C in water and to 3493 cm^{-1} after heating to 300 °C. Upon acetic acid adsorption, a weak band appeared at 2461 cm^{-1} and remained in the spectra after the rinsing of the acetic acid-saturated 13X in distilled water and heating at 300 °C. A characteristic broad feature in the range 3300–2500 cm^{-1}, that overlaps the C–H stretching region, and with a secondary absorption close to 2600 cm^{-1}, is observed for the hydrogen-bonded O–H of most carboxylic acids. Other bands that are associated with the C–O and O–H components of the carboxylic acid tend to be less pronounced, and sometimes may be overlapped with other fingerprint absorptions of the molecule. These are located in the ranges 1320–1210 cm^{-1} (C–O stretch) and 960–850 cm^{-1} (hydrogen-bonded O–H out-of-plane bending) (96).

Formation of acetate ions in NaHY was explained by the following reaction (99):

$$\text{zeol–OH} + \text{HOOC–CH}_3 \rightarrow \text{zeol–OH}_2^+ + {}^-\text{OOC–CH}_3 \rightarrow \text{zeol}^+ + {}^-\text{OOC–CH}_3 + \text{H}_2\text{O}$$

Upon the adsorption of acetic acid vapor on NaHY at 200 °C resulted in the removal of first 3640 cm^{-1} band (high frequency band, typical of Si–O1H–Al situated inside supercages) and then 3550 cm^{-1} band (low frequency band, typical of Si–O3H–Al situated inside hexagonal prisms). However in the same study interaction of acetic acid vapor with Na^+ ions in NaY did not result in any important variation of the spectrum of the acetic acid solution suggesting molecular adsorption of acetic acid in NaY. For NaY which usually does not contain Si–OH–Al groups, the acetate ions were actually not formed. A small number of acetate ions formed in NaY was related to the presence of very small amounts of extra framework Al species and/or a very small amount of Si–OH–Al formed by the hydrolysis of NaY (99).

The shift of the 3506 cm^{-1} band to lower wavenumbers upon acetic acid adsorption and to higher wavenumbers upon heating at 300 °C can be explained by the increased and decreased strength of the water or acetic acid–framework oxygen hydrogen bonds, respectively. Beta and co-workers observed a correlation between the position of the broad band at about 3400–3500 cm^{-1} (assigned to O–H stretchings of water molecules hydrogen bonded to framework oxygen) and the basicity of framework oxygen atoms of NaX. The frequency of this band decreased with decreasing water loading suggesting formation of more strongly bonded water-cation clusters as a significant number of water molecules was removed (107).

The surface of the framework of 13X is essentially oxygen atoms, whereas Si and Al are buried or recessed in the tetrahedra of oxygen atoms. They therefore are not fully exposed and cannot be readily accessed by adsorbate molecules. Also, the anionic oxygen atoms are more abundant and are much more polarizable than the Al and Si cations (79). In 13X, the framework oxygen atoms which bear the negative charge of the lattice are considered as the structural basic sites. Basic sites on oxide surfaces may be constituted by surface OH_s^- or O_s^{2-} anions. Acids which

contain H-X functions are expected to undergo H-bonding interactions with basic surface sites (111):

$$O_s^{2-} + H{-}X \leftrightarrows O_s^{2-}\cdots H{-}X$$

For weak interactions, the H-bond characteristics are the same as in the case of basic probe molecules interacting with Brønsted acid sites. Therefore, frequency shifts of the H-X stretching mode in the H-bonded complex relative to the free acid molecule must be induced and line broadening and intensity enhancements must also occur (111).

Thermogravimetric and IR spectroscopic studies of acetic acid adsorbed on faujasite-type zeolites for the characterization of the strength and catalytic behavior of base centres have been reported in the literature (97, 112, 113). Przystajko and co-workers determined distributions of base strengths using indicator techniques and infrared spectroscopic studies of acetic acid vapor adsorbed on faujasite-type zeolites. The infrared spectra in the region of wavenumbers below 1200 cm^{-1} were also examined since removal of aluminum from the lattice is reflected by a shift of the bands in this region towards higher frequencies. The aluminum atoms removed from the lattice and present as extralattice aluminum can be present in the form of species contributing to sample basicity. It was shown that the lattice $(AlO_4)^-$ tetrahedra or oxide anions of these tetrahedral (Lewis type basicity) played the role of base sites in the sodium forms of X and Y type zeolites (112).

In the present study, the bands detected in the 1200–1800 cm^{-1} after the acetic acid adsorption indicated that adsorption of acetic acid in 13X resulted in formation of acetic acid ions (acetate, CH_3COO^-). For 13X which usually does not contain Si–OH–Al groups, formation of the acetate ions was not expected (99). However it was reported that NaX does not contain a total exchange cation equivalency due to partial hydrolysis of the Na^+ cations and replacement by hydronium ions. This cation deficient form of NaX may exhibit properties associated with hydroxyl groups (86). Thus the formation of the acetate ions in 13X in the present study can be related to presence of extraframework Al species and/or Si–OH–Al formed by the hydrolysis of 13X (99). However it was not possible to follow the changes in the bands in the O–H stretching and H–O–H bending regions upon the adsorption/desorption treatments performed since presence of water in 13X complicated interpretation of the bands in these regions. The broad band in the O–H stretching region of the hydrated 13X completely blanked out the spectral region.

In the literature Zhang and co-workers did not reported obvious changes in the SEM micrographs and XRD patterns after interaction of 5 g of 13X zeolite ($SiO_2/Al_2O_3<3$, in pellet and powder forms) with 100 mL of aqueous acetic acid solutions with the initial concentrations of 0.076–0.901 mol/L. The results verified that the 13X was stable when exposed to dilute acetic

acid solution (60). Considering the lower initial concentrations of the acetic acid solutions (0.028-0.544 mol/L) and lower adsorbent/solution ratio (2 g/100 mL) in the present study it is expected that the 13X has chemical stability in the dilute acetic acid solutions.

CONCLUSION

It was shown that the kinetics of adsorption of acetic acid from diluted acetic acid solutions might be represented by the pseudo-second order model and the model parameters were determined. The adsorbed amount of acetic acid at equilibrium was decreased with the increasing adsorption temperature. The adsorption equilibrium data was best described by the Sips model and the model parameters were determined. The Sips model parameter characterizing the system heterogeneity was found to decrease with the increased temperature. From the temperature dependence of the Sips model adsorption affinity constant the isosteric heat at the fractional loading of 0.5 was calculated as 50.40 kJ/mol. The monolayer acetic acid adsorption capacity of 13X at 25 °C was calculated as 6.32 mmol/g. The dimensionless separation factor values were found to vary within the range of 0.026–0.434 indicating the favorable adsorption. The negative ΔG° values indicated spontaneous adsorption of acetic acid on 13X zeolite. The positive ΔH° values designated that the sorption of acetic acid in 13X was endothermic. However, as previously stated, the amount of acetic acid adsorbed at equilibrium decreased with the increasing temperature. The reason for that in the low acetic acid concentration range in which the dimensionless adsorption equilibrium constant was calculated the amount of acetic acid adsorbed at equilibrium increased with temperature. The positive values of entropy change was implied the increased randomness (degree of freedom of the system) at the solid-solute interface during adsorption. FTIR studies were revealed that the acetic acid adsorption was resulted in formation of acetate ions. It was not possible desorb all the species formed by rinsing the acid-saturated 13X in distilled water at 45°C or by heating at 300°C in air although removal of some species was observed by FTIR spectroscopy.

ACKNOWLEDGEMENTS

The study presented here was perfomed as Graduation Project in 2015-16 Spring Term in Department of Chemical Engineering, Uşak University. Part of the study was presented as a poster in 12nd National Chemical Engineering Congress (23–26 August 2016, İzmir) and was published in the Book of Proceedings. The author thanks to Burak Ertugrul and M. Murat Tercanli for their help in the experimental work.

REFERENCES

1. Huang RYM, Moreira A, Notarfonzo R, Xu YF. Pervaporation Separation of Acetic Acid-Water Mixtures Using Modified Membranes .1. Blended Polyacrylic-Acid (Paa)-Nylon 6 Membranes. J Appl Polym Sci. 1988 Apr;35(5):1191-200. PubMed PMID: WOS:A1988M893700006. English.

2. C. Le Berre PS, P. Kalck, G.P. Torrence. Acetic Acid. Ullmann's Encyclopedia of Industrial Chemistry. Weinheim: Wiley-VCH Verlag GmbH & Co. KGaA; 2013.

3. King CJ. Acetic Acid Extraction. In: Lo TC, Baird,M. H. I., Hanson, C., editor. Handbook of Solvent Extraction: Wiley; 1983. p. 567-72.

4. http://www.essentialchemicalindustry.org/chemicals/ethanoic-acid.html.

5. Lopez-Garzon CS, Straathof AJJ. Recovery of carboxylic acids produced by fermentation. Biotechnol Adv. 2014 Sep-Oct;32(5):873-904. PubMed PMID: WOS:000340696900001. English.

6. Palasantzas IA, Wise DL. Preliminary Economic-Analysis for Production of Calcium-Magnesium Acetate from Organic Residues. Resour Conserv Recy. 1994 Jun 30;11(1-4):225-43. PubMed PMID: WOS:A1994NY74000020. English.

7. Han IS, Cheryan M. Downstream processing of acetate fermentation broths by nanofiltration. Appl Biochem Biotech. 1996 Spr;57-8:19-28. PubMed PMID: WOS:A1996UL85700004. English.

8. Straathof AJJ. Transformation of biomass into commodity chemicals using enzymes or cells. Chem Rev. 2014;114(3):1871-908.

9. Hong YK, Hong WH. Removal of acetic acid from aqueous solutions containing succinic acid and acetic acid by tri-n-octylamine. Sep Purif Technol. 2005 Mar 15;42(2):151-7. PubMed PMID: WOS:000227589900008. English.

10. Rasrendra CB, Girisuta B, van de Bovenkamp HH, Winkelman JGM, Leijenhorst EJ, Venderbosch RH, et al. Recovery of acetic acid from an aqueous pyrolysis oil phase by reactive extraction using tri-n-octylamine. Chem Eng J. 2011 Dec 1;176:244-52. PubMed PMID: WOS:000298900200033. English.

11. Keshav A, Wasewar KL, Chand S. Extraction of Propionic Acid From Model Solutions: Effect of pH, Salts, Substrate, and Temperature. Aiche J. 2009 Jul;55(7):1705-11. PubMed PMID: WOS:000267475700008. English.

12. Liu L, Zhu YF, Li JH, Wang M, Lee P, Du GC, et al. Microbial production of propionic acid from propionibacteria: Current state, challenges and perspectives. Crit Rev Biotechnol. 2012 Dec;32(4):374-81. PubMed PMID: WOS:000310708100005. English.

13. King CJ. Amine-Based Systems for Carboxylic-Acid Recovery. Chemtech. 1992 May;22(5):285-91. PubMed PMID: WOS:A1992HU32900007. English.

14. Li SG, Tuan VA, Noble RD, Falconer JL. A Ge-substituted ZSM-5 zeolite membrane for the separation of acetic acid from water. Ind Eng Chem Res. 2001 Dec 26;40(26):6165-71. PubMed PMID: WOS:000172916100016. English.

15. Sircar S, inventor; Air Products and Chemicals, Inc., assignee. Separation of liquid mixtures by concentration swing adsorption patent 5,026,482. 1991.

16. Kim GH, Park SJ, Um BH. Response surface methodology for optimization of solvent extraction to recovery of acetic acid from black liquor derived from Typha latifolia pulping process. Ind Crop Prod. 2016 Oct 30;89:34-44. PubMed PMID: WOS:000381231000006. English.

17. Ahsan L, Jahan MS, Ni YH. Recovery of Acetic Acid from the Prehydrolysis Liquor of Kraft Based Dissolving Pulp Production Process: Sodium Hydroxide Back Extraction from the Trioctylamine/Octanol System. Ind Eng Chem Res. 2013 Jul 3;52(26):9270-5. PubMed PMID: WOS:000321541600064. English.

18. Yang G, Jahan MS, Ahsan L, Zheng LQ, Ni YH. Recovery of acetic acid from pre-hydrolysis liquor of hardwood kraft-based dissolving pulp production process by reactive extraction with triisooctylamine. Bioresource Technol. 2013 Jun;138:253-8. PubMed PMID: WOS:000320296600033. English.

19. Datta D, Kumar S, Uslu H. Status of the Reactive Extraction as a Method of Separation. J Chem-Ny. 2015. PubMed PMID: WOS:000352907900001. English.

20. Henczka M, Djas M. Reactive extraction of acetic acid and propionic acid using supercritical carbon dioxide. J Supercrit Fluid. 2016 Apr;110:154-60. PubMed PMID: WOS:000370902300017. English.

21. Samanta HS, Ray SK, Das P, Singha NR. Separation of acid-water mixtures by pervaporation using nanoparticle filled mixed matrix copolymer membranes. J Chem Technol Biot. 2012 May;87(5):608-22. PubMed PMID: WOS:000302463000004. English.

22. Sun WG, Wang XW, Yang JH, Lu JM, Han HL, Zhang Y, et al. Pervaporation separation of acetic acid-water mixtures through Sn-substituted ZSM-5 zeolite membranes. J Membrane Sci. 2009 Jun 15;335(1-2):83-8. PubMed PMID: WOS:000266057600013. English.

23. Moulik S, Nazia S, Vani B, Sridhar S. Pervaporation separation of acetic acid/water mixtures through sodium alginate/polyaniline polyion complex membrane. Sep Purif Technol. 2016 Oct 1;170:30-9. PubMed PMID: WOS:000381950300004. English.

24. Kulkarni SS, Tambe SM, Kittur AA, Kariduraganavar MY. Preparation of novel composite membranes for the pervaporation separation of water-acetic acid mixtures. J Membrane Sci. 2006 Nov 15;285(1-2):420-31. PubMed PMID: WOS:000242209000046. English.

25. Yu J, Li H, Liu HZ. Recovery of acetic acid over water by pervaporation with a combination of hydrophobic ionic liquids. Chem Eng Commun. 2006;193(11):1422-30. PubMed PMID: WOS:000239382500006. English.

26. Kittur AA, Tambe SM, Kulkarni SS, Kariduraganavar MY. Pervaporation separation of water-acetic acid mixtures through NaY zeolite-incorporated sodium alginate membranes. J Appl Polym Sci. 2004 Dec 5;94(5):2101-9. PubMed PMID: WOS:000224759700032. English.

27. Sano T, Ejiri S, Yamada K, Kawakami Y, Yanagishita H. Separation of acetic acid-water mixtures by pervaporation through silicalite membrane. J Membrane Sci. 1997;123(2):225-33.

28. Netke SA, Sawant SB, Joshi JB, Pangarkar VG. Sorption and Permeation of Acetic-Acid through Zeolite Filled Membrane. J Membrane Sci. 1995 Nov 15;107(1-2):23-33. PubMed PMID: WOS:A1995TF98100002. English.

29. Yamanaka N, Itakura M, Kiyozumi Y, Ide Y, Sadakane M, Sano T. Acid stability evaluation of CHA-type zeolites synthesized by interzeolite conversion of FAU-type zeolite and their membrane application for dehydration of acetic acid aqueous solution. Micropor Mesopor Mat. 2012 Aug 1;158:141-7. PubMed PMID: WOS:000305714200018. English.

30. Baruah K, Hazarika S. Separation of Acetic Acid from Dilute Aqueous Solution by Nanofiltration Membrane. J Appl Polym Sci. 2014 Aug 5;131(15). PubMed PMID: WOS:000336456400058. English.

31. Lu SY, Chiu CP, Huang HY. Pervaporation of acetic acid/water mixtures through silicalite filled polydimethylsiloxane membranes. J Membrane Sci. 2000 Aug 20;176(2):159-67. PubMed PMID: WOS:000088820400002. English.

32. Deng SZ, Sourirajan S, Matsuura T. A Study of Polydimethylsiloxane Aromatic Polyamide Laminated Membranes for Separation of Acetic-Acid Water Mixtures by Pervaporation Process. Sep Sci Technol. 1994;29(9):1209-16. PubMed PMID: WOS:A1994NT66200007. English.

33. Yoshikawa M, Kuno S, Wano T, Kitao T. Specialty Polymeric Membranes .4. Pervaporation Separation of Acetic-Acid Water Mixtures through Modified Polybutadiene Membranes. Polym Bull. 1993 Nov;31(5):607-13. PubMed PMID: WOS:A1993MH90800015. English.

34. Liu Q, Noble RD, Falconer JL, Funke HH. Organics/water separation by pervaporation with a zeolite membrane. J Membrane Sci. 1996 Aug 21;117(1-2):163-74. PubMed PMID: WOS:A1996UZ77500012. English.

35. Yu LX, Guo QF, Hao JH, Jiang WJ. Recovery of acetic acid from dilute wastewater by means of bipolar membrane electrodialysis. Desalination. 2000 Aug 10;129(3):283-8. PubMed PMID: WOS:000088625900008. English.

36. Rehouma A, Belaissaoui B, Hannachi A, Muhr L. Bipolar membrane electrodialysis and ion exchange hybridizing for dilute organic acid solutions treatment. Desalin Water Treat. 2013 Jan;51(1-3):511-7. PubMed PMID: WOS:000313790300056. English.

37. Chukwu U, Cheryan M. Concentration of vinegar by electrodialysis. J Food Sci. 1996 Nov-Dec;61(6):1223-6. PubMed PMID: WOS:A1996VZ33400026. English.

38. Jia YX, Chen X, Wang M, Wang BB. A win-win strategy for the reclamation of waste acid and conversion of organic acid by a modified electrodialysis. Sep Purif Technol. 2016 Oct 17;171:11-6. PubMed PMID: WOS:000383313300002. English.

39. Yu LX, Lin T, Guo QF, Hao JH. Relation between mass transfer and operation parameters in the electrodialysis recovery of acetic acid. Desalination. 2003 Apr 15;154(2):147-52. PubMed PMID: WOS:000181363500005. English.

40. Van der Bruggen B, Manttari M, Nystrom M. Drawbacks of applying nanofiltration and how to avoid them: A review. Sep Purif Technol. 2008 Oct 22;63(2):251-63. PubMed PMID: WOS:000260702600003. English.

41. Ganguly SK, Goswami AN. Surface diffusion kinetics in the adsorption of acetic acid on activated carbon. Sep Sci Technol. 1996;31(9):1267-78. PubMed PMID: WOS:A1996UL35200005. English.

42. Munson CL, Garcia AA, Kuo Y, Frierman M, King CJ. Use of Adsorbents for Recovery of Acetic Acid From Aqueous Solutions Part II – Factors Governing Selectivity. Separation & Purification Reviews. 1987;16(1):65-89.

43. Frierman M, Kuo Y, Joshi D, Garcia AA, King CJ. Use of Adsorbents for Recovery of Acetic-Acid from Aqueous-Solutions .3. Solvent Regeneration. Separ Purif Method. 1987;16(1):91-102. PubMed PMID: WOS:A1987J686500004. English.

44. Munson CL, Garcia AA, Kuo Y, Frierman M, King CJ. Use of Adsorbents for Recovery of Acetic-Acid from Aqueous-Solutions .2. Factors Governing Selectivity. Separ Purif Method. 1987;16(1):65-89. PubMed PMID: WOS:A1987J686500003. English.

45. Kuo Y, Munson CL, Rixev WG, Garcia AA, Frierman M, King CJ. Use of Adsorbents For Recovery of Acetic Acid From Aqueous Solutions Part I – Factors Governing Capacity. Separation & Purification Reviews. 1987;16(1):31-64.

46. Park KM, Nam HG, Mun S. Adsorption equilibria of acetic acid on activated carbon. Korean Chemical Engineering Research. 2015;53(1):127-30.

47. Lopez-Velandia C, Moreno-Barbosa JJ, Sierra-Ramirez R, Giraldo L, Moreno-Pirajan JC. Adsorption of Volatile Carboxylic Acids on Activated Carbon Synthesized from Watermelon Shells. Adsorpt Sci Technol. 2014;32(2-3):227-42. PubMed PMID: WOS:000336237000011. English.

48. Dina DJD, Ntieche, A.R., Ndi, J.N., Ketcha Mbadcam J., . Adsorption of Acetic acid onto Activated Carbons obtained from Maize cobs by Chemical Activation with Zinc chloride (ZnCl2). Research Journal of Chemical Sciences. 2012;2(9):42-9.

49. Frierman M, Kuo Y, Joshi D, Garcia AA, King CJ. Use of Adsorbents for Recovery of Acetic Acid From Aqueous Solutions Part Iii -- Solvent Regeneration. Separation & Purification Reviews. 1987;16(1):91-102.

50. Garcia AA, King CJ. Use of basic polymer sorbents for the recovery of acetic acid from dilute aqueous solution. Industrial and Engineering Chemistry Research. 1989;28(2):204-12.

51. Gustafson RL, Albright RL, Heisler J, Lirio JA, Reid Jr OT. Adsorption of organic species by high surface area styrene-divinylbenzene copolymers. Industrial and Engineering Chemistry Product Research and Development. 1968;7(2):107-15.

52. Gregory J, Semmens MJ. Sorption of carboxylate ions by strongly basic anion exchangers. Journal of the Chemical Society, Faraday Transactions 1: Physical Chemistry in Condensed Phases. 1972;68:1045-52.

53. Narges SL. Study of the Adsorption of Acetic Acid on Silica Gel in Aqueous Solution. Rev Roum Chim. 2013 Jan;58(1):43-+. PubMed PMID: WOS:000329771100006. English.

54. Morad Y, Hilali, M., Bazzi, L., Chaway, A. Elimination of organic pollutant (Acetic acid) by adsorption on clays in aqueous solution: kinetic study and adsorption isotherms. Physical Chemistry: An Indian Journal 2014 2014;9(1):8-14.

55. Akbar S, Punnathanam, S., Pukala, M., . Adsorption of aqueous solutions of carboxylic acids on montmorillonite, silicate, H-ZSM-5 and their Na+- and Li+-exchanged forms. Journal of The Chemical Society Of Pakistan. 2008;30(5):664-73.

56. Ozcan O, Inci I, Asci YS. Multiwall Carbon Nanotube for Adsorption of Acetic Acid. J Chem Eng Data. 2013 Mar;58(3):583-7. PubMed PMID: WOS:000316307800010. English.

57. Bowen TC, Vane LM. Ethanol, acetic acid, and water adsorption from binary and ternary liquid mixtures on high-silica zeolites. Langmuir. 2006 Apr 11;22(8):3721-7. PubMed PMID: WOS:000236745700043. English.

58. Efe C, Van Der Wielen LAM, Straathof AJJ. High silica zeolites as an alternative to weak base adsorbents in succinic acid recovery. Industrial and Engineering Chemistry Research. 2010;49(4):1837-43.

59. Faisal A, Zarebska A, Saremi P, Korelskiy D, Ohlin L, Rova U, et al. MFI zeolite as adsorbent for selective recovery of hydrocarbons from ABE fermentation broths. Adsorption. 2014;20(2-3):465-70.

60. Zhang HH, Wang YM, Bai P, Guo XH, Ni XX. Adsorptive Separation of Acetic Acid from Dilute Aqueous Solutions: Adsorption Kinetic, Isotherms, and Thermodynamic Studies. J Chem Eng Data. 2016 Jan;61(1):213-9. PubMed PMID: WOS:000368564600025. English.

61. Zhang HH, Lan XY, Bai P, Guo XH. Adsorptive removal of acetic acid from water with metal-organic frameworks. Chemical Engineering Research & Design. 2016 Jul;111:127-37. PubMed PMID: WOS:000380624300011. English.

62. Lipnizki F, Field RW, Ten PK. Pervaporation-based hybrid process: a review of process design, applications and economics. Journal of Membrane Science. 1999 Feb 17;153(2):183-210. PubMed PMID: WOS:000078138100005. English.

63. Feng XS, Huang RYM. Liquid separation by membrane pervaporation: A review. Ind Eng Chem Res. 1997 Apr;36(4):1048-66. PubMed PMID: WOS:A1997WR40200006. English.

64. Fleming HL. Consider membrane pervaporation. Chemical engineering progress. 1992;88(7):46-52.

65. Huang RY. Pervaporation membrane separation processes: Elsevier Science Ltd; 1991.

66. Morigami Y, Kondo M, Abe J, Kita H, Okamoto K. The first large-scale pervaporation plant using tubular-type module with zeolite NaA membrane. Sep Purif Technol. 2001 Oct 1;25(1-3):251-60. PubMed PMID: WOS:000171837900026. English.

67. Li G, Kikuchi E, Matsukata M. Separation of water-acetic acid mixtures by pervaporation using a thin mordenite membrane. Sep Purif Technol. 2003;32(1-3):199-206.

68. Casado L, Mallada R, Téllez C, Coronas Jn, Menéndez M, Santamaría J. Preparation, characterization and pervaporation performance of mordenite membranes. Journal of Membrane Science. 2003;216(1):135-47.

69. Li G, Kikuchi E, Matsukata M. A study on the pervaporation of water-acetic acid mixtures through ZSM-5 zeolite membranes. J Membrane Sci. 2003;218(1-2):185-94.

70. Masuda T, Otani S, Tsuji T, Kitamura M, Mukai SR. Preparation of hydrophilic and acid-proof silicalite-1 zeolite membrane and its application to selective separation of water from water solutions of concentrated acetic acid by pervaporation. Sep Purif Technol. 2003;32(1-3):181-9.

71. Lagergren S. About the theory of so-called adsorption of soluble substances. 1898.

72. Ho YS, McKay G. Pseudo-second order model for sorption processes. Process Biochemistry. 1999 Jul;34(5):451-65. PubMed PMID: WOS:000081912700005. English.

73. Weber WJ, Morris JC. Kinetics of adsorption on carbon from solution. Journal of the Sanitary Engineering Division. 1963;89(2):31-60.

74. Do DD. Adsorption Analysis: Equilibria and Kinetics:(With CD Containing Computer Matlab Programs): World Scientific; 1998.

75. Lv HS, Sun YP, Zhang MH, Geng ZF, Ren MM. Removal of Acetic Acid from Fuel Ethanol Using Ion-Exchange Resin. Energy & Fuels. 2012 Dec;26(12):7299-307. PubMed PMID: WOS:000312516400026. English.

76. Weber TW, Chakravorti RK. Pore and solid diffusion models for fixed-bed adsorbers. AIChE Journal. 1974;20(2):228-38.

77. McKay G, Blair HS, Gardner JR. Adsorption of dyes on chitin. I. Equilibrium studies. J Appl Polym Sci. 1982;27(8):3043-57.

78. Hansen RS, Craig RP. The adsorption of aliphatic alcohols and acids from aqueous solutions by non-porous carbons. The Journal of Physical Chemistry. 1954;58(3):211-5.

79. Yang RT. Zeolites and Molecular Sieves. Adsorbents: Fundamentals and Applications: John Wiley & Sons, Inc.; 2003. p. 157-90.

80. Dubinin M, Radushkevich L. Equation of the characteristic curve of activated charcoal. Chem Zentr. 1947;1(1):875.

81. Svilović S, Rušić D, Žanetić R. Thermodynamics and adsorption isotherms of copper ions removal from solutions using synthetic zeolite X. Chemical and Biochemical Engineering Quarterly. 2008;22(3):299-305.

82. Arslan A, Veli S. Zeolite 13X for adsorption of ammonium ions from aqueous solutions and hen slaughterhouse wastewaters. Journal of the Taiwan institute of chemical engineers. 2012;43(3):393-8.

83. Quintelas C, Pereira R, Kaplan E, Tavares T. Removal of Ni (II) from aqueous solutions by an Arthrobacter viscosus biofilm supported on zeolite: from laboratory to pilot scale. Bioresource Technol. 2013;142:368-74.

84. Kim B, Lee H, Moon H, Lee K. Adsorption of radionuclides from aqueous solutions by inorganic adsorbents. Separation science and technology. 1995;30(16):3165-82.

85. Dubinin M. The potential theory of adsorption of gases and vapors for adsorbents with energetically nonuniform surfaces. Chemical Reviews. 1960;60(2):235-41.

86. Breck DW. Zeolite Molecular Sieves: Structure, Chemistry and Use1974. null p.

87. Jung BK, Hasan Z, Jhung SH. Adsorptive removal of 2,4-dichlorophenoxyacetic acid (2,4-D) from water with a metal-organic framework. Chem Eng J. 2013 Dec;234:99-105. PubMed PMID: WOS:000328588300013. English.

88. Lin S, Song Z, Che G, Ren A, Li P, Liu C, et al. Adsorption behavior of metal–organic frameworks for methylene blue from aqueous solution. Micropor Mesopor Mat. 2014;193:27-34.

89. Blake P, Jackson G. The thermal decomposition of acetic acid. Journal of the Chemical Society B: Physical Organic. 1968:1153-5.

90. Bamford C, Dewar M. 608. The thermal decomposition of acetic acid. Journal of the Chemical Society (Resumed). 1949:2877-82.

91. Sigma-Aldrich. 13X product information sheet [cited 2017 01 Feb]. Available from: https://www.sigmaaldrich.com/content/dam/sigma-aldrich/docs/Sigald/Product_Information_Sheet/1/208582pis.pdf.

92. Stumm W, Morgan JJ. Aquatic Chemistry: Chemical Equilibria and Rates in Natural Waters {Environmental Science and Technology}: Wiley; 1996.

93. Van Santen R, Vogel D. Lattice dynamics of zeolites. Adv Solid-State Chem. 1989;1:151-224.

94. Jacobs W, Van Wolput J, Van Santen R. An in situ Fourier transform infrared studyof zeolitic vibrations: Dehydration, deammoniation, and reammoniation of ion-exchanged Y zeolites. Zeolites. 1993;13(3):170-82.

95. Pichat P, Beaumont R, Barthomeuf D. Infra-red structural study of aluminium-deficient Y zeolites. Journal of the Chemical Society, Faraday Transactions 1: Physical Chemistry in Condensed Phases. 1974;70:1402-7.

96. Coates J. Interpretation of infrared spectra, a practical approach. Encyclopedia of analytical chemistry. 2000.

97. Bielański A, Datka J. Amphiprotic properties of OH groups in synthetic NaHY zeolites. Journal of Catalysis. 1974;32(2):183-9.

98. Kubicki J, Schroeter L, Itoh M, Nguyen B, Apitz S. Attenuated total reflectance Fourier-transform infrared spectroscopy of carboxylic acids adsorbed onto mineral surfaces. Geochim Cosmochim Ac. 1999;63(18):2709-25.

99. Kukulska-Zajac E, Gora-Marek K, Datka J. IR and TPD studies of the reaction of acetic acid in zeolites NaHY. Micropor Mesopor Mat. 2006 Nov 26;96(1-3):216-21. PubMed PMID: WOS:000242229200030. English.

100. Ma YN, Yan CJ, Alshameri A, Qiu XM, Zhou CY, Li D. Synthesis and characterization of 13X zeolite from low-grade natural kaolin. Adv Powder Technol. 2014 Mar;25(2):495-9. PubMed PMID: WOS:000334729500004. English.

101. Liu X. Infrared and Raman spectroscopy. Zeolite Characterization and Catalysis: Springer; 2009. p. 197-222.

102. Uytterhoeven J, Schoonheydt R, Liengme B, Hall WK. Studies of the hydrogen held by solids: XVI. Infrared spectroscopy of X-and Y-type zeolites containing univalent and divalent cations. Journal of Catalysis. 1969;13(4):425-34.

103. Jacobs P, Uytterhoeven J. Assignment of the hydroxyl bands in the infrared spectra of zeolites X and Y. Part 1.—Na—H zeolites. Journal of the Chemical Society, Faraday Transactions 1: Physical Chemistry in Condensed Phases. 1973;69:359-72.

104. Carter J, Lucchesi P, Yates D. The nature of residual OH groups on a series of near-faujasite zeolites. The Journal of Physical Chemistry. 1964;68(6):1385-91.

105. de Mallmann A, Barthomeuf D. Change in benzene adsorption with acidobasicity of (Cs,Na)X zeolites studied by i.r. spectroscopy. Zeolites. 1988 1988/07/01;8(4):292-301.

106. Bertsch L, Habgood H. An infrared spectroscopic study of the adsorption of water and carbon dioxide by Linde molecular sieve X1. The Journal of Physical Chemistry. 1963;67(8):1621-8.

107. Beta IA, Bohlig H, Hunger B. Structure of adsorption complexes of water in zeolites of different types studied by infrared spectroscopy and inelastic neutron scattering. Physical Chemistry Chemical Physics. 2004;6(8):1975-81.

108. Angell CL, Schaffer PC. Infrared Spectroscopic Investigations of Zeolites and Adsorbed Molecules. I. Structural OH Groups1. The Journal of Physical Chemistry. 1965 1965/10/01;69(10):3463-70.

109. Hunger J, Beta IA, Böhlig H, Ling C, Jobic H, Hunger B. Adsorption Structures of Water in NaX Studied by DRIFT Spectroscopy and Neutron Powder Diffraction. The Journal of Physical Chemistry B. 2006 2006/01/01;110(1):342-53.

110. Martra G, Coluccia S, Davit P, Gianotti E, Marchese L, Tsuji H, et al. Acidic and basic sites in NaX and NaY faujasites investigated by NH3, CO2 and CO molecular probes. Research on Chemical Intermediates. 1999;25(1):77-93.

111. Knözinger H, Huber S. IR spectroscopy of small and weakly interacting molecular probes for acidic and basic zeolites. Journal of the chemical society, faraday transactions. 1998;94(15):2047-59.

112. Przystajko W, Fiedorow R, Dalla Lana IG. Base properties of zeolite catalysts. Zeolites. 1987 9//;7(5):477-81.

113. Ciambelli P, Corbo P. Acid-base properties of zeolites by acetic acid temperature programmed desorption. Thermochim Acta. 1988;137(1):51-8.

JOTCS B
Journal of the Turkish Chemical Society
Section: B
Chemical Engineering
TURKISH CHEMICAL SOCIETY

CRYSTALLINE STARCH CITRATE BIOPOLYMER NANORODS AS POTENTIAL STABILIZERS IN NANO AND MICRO EMULSIONS

Oluwaseyi D. Saliu, Gabriel A. Olatunji, Oluwatoyin O. Ajetomobi, Adebayo I. Olosho, Idowu Abiodun, Gbenga Amusan

Department of Industrial Chemistry, University of Ilorin, Ilorin, Nigeria

Abstract: The area of green chemistry which involves the synthesis of biodegradable polymers with better stabilizing properties is fast-developing. Starch biopolymer was citrate modified and converted to crystalline nanorods through green methods and was fully characterized using the fourier transform infrared spectroscopy (FTIR), scanning electron microscopy (SEM), transmission electron microscopy (TEM) and thermogravimetric analysis (TGA). The crystalline starch citrate showed better morphological and thermal stability properties than the ordinary and modified normal starch which has not been converted to nano form. The TGA result revealed a single step thermal degradation at 240 to 410 °C and percentage weight loss of about 89%. The SEM and TEM also confirmed the synthesis of rod-like or cylindrical nanoparticles with little or no aggregation. This property coupled with the thermal stability makes starch citrate nanoparticles a good stabilizer for nano and micro emulsions.

Keywords: Starch citrate, nanoparticles, stabilizer, biopolymers.

Submitted: June 2, 2017. **Accepted:** November 10, 2017.

Cite this: Saliu OD, Olatunji G, Ajetomobi O, Olosho A, Abiodun I, Amusan G. CRYSTALLINE STARCH CITRATE BIOPOLYMER NANORODS AS POTENTIAL STABILIZERS IN NANO AND MICRO EMULSIONS. JOTCSB. 2017;1(2):191–200.

***Corresponding author. E-mail:** oluwaseyi229@gmail.com

INTRODUCTION

The most abundant forms of biodegradable polymer which include cellulose, starch, and chitin have become the major point of interest of researchers in the field of material chemistry (1). These biodegradable biopolymers which find diverse applications in medicine, pharmacy, chemistry and other major field of science are chosen because of their biocompatibility, biodegradability, and availability (2, 3). Polysaccharides are known to occupy a larger space in the world of biodegradable polymers and are well known for their versatility in sensing, drug delivery, tissue engineering applications (4) because of the recognition, stabilization and catalytic properties that they possess due to the presence of available hydroxyl groups that can interact with other organic and inorganic hydrophilic or hydrophobic groups in reaction media (5, 6).

Starch occurs as a biodegradable, non-toxic, biocompatible semi-crystalline granule which is made up of about 70% branched amylopectin and about 30% linear amylase and it is one of the most available biopolymers in the universe with its application extent depending on the degree of modification and processing it has passed through (7). Processing operations like gelatinization, retro-gradation, gel formation and crystallization which modifies the internal bonding system and degree of substitution of starch tend to affect the quality and performance of starch for application in industrial sectors (8). Although, these hydrophilic properties inherent in starch biopolymers makes it difficult for the synthesis or growth of starch nanoparticles and there is therefore a need to either increase the hydrophobic content of starch by grafting it with hydrophobic addenda or by developing nano-precipitation techniques for synthesizing of hydrophilic starch nanoparticles in less toxic organic reagents (9).

There are earlier reports on the synthesis of starch nanoparticles by a complex formation between starch and butanol but the significant loss in yield which plagues this method due to the hydrolytic process involved creates a major setback on the use of the technique (10, 11). Although a better method with almost 100 percent yield which involved a high pressure homogenization has been reported for corn starches but this method lacks reproducibility (12). The method which gave both high yield and reproducibility is the nano-precipitation technique which has already been successful for the synthesis of nano forms of poly (lactic acid) and poly (lactic-co-glycolic acid) and is also been recently used for the synthesis of starch nanoparticles (4). This nano-precipitation technique involves a simultaneous emulsification and diffusion technique is easy to scale up for industrial purposes and it gives avenue for starch nanoparticle size and shape control, stability and modification (13, 14).

Nanoemulsions are unstable colloidal dispersions in which at least one of the two immiscible liquids which form the dispersion has its diameter in the range of twenty to two hundred nanometers (15, 16). These nanoemulsions with their oil phase homogenized into aqueous phase have a thermodynamic stability which depends on the nature and concentration of stabilizers and emulsifiers used. They are used to encapsulate poorly soluble drugs and food bioactives for safe delivery to the site of interests (17, 18). The citric acid treatment of ordinary starch or starch nanoparticles expands the application of starch biopolymers in the area of stabilization of nano or micro emulsions (19). Starch citrate which is generally regarded as a form of resistant starch, it does not swell and gelatinize in hot water conditions, hence it can be conveniently used as stabilizers and reinforcements in both cold and hot conditions (7, 20).

The major improvement which citric acid modifications gives starch nanoparticles is that it improves their thermal stability and interfacial tension properties (1) for enhanced performance as good stabilizers or emulsifiers in any nano and micro emulsions produced either in cold or hot reaction conditions (21, 22). The citrate derivatives of starch can be used as structure-directing agents in synthesis of transition metal nanoparticles, directly compressible recipients in tablet formulations and heavy metal adsorbents in polluted or contaminated effluents (7). Hence, the purpose of this research is to synthesize starch nanoparticles with stable shapes and to modify with citric acid so as to improve their thermal, stabilization and emulsification properties in nano and micro emulsions.

MATERIALS AND METHOD

Water-soluble maize starch and citric acid were obtained from Sigma Aldrich, USA. All reagents used were of analytical grade and further purifications were not carried out.

Synthesis of starch nanoparticles

The method of Chin *et al*. was adopted and slightly modified. Starch nanoparticles were dissolved in NaOH/urea (NU) (0.8:1 wt %) solution mixture and introduced into excess absolute ethanol under controlled conditions. In general, 1 wt % native starch solution was prepared by dissolving native starch powder in the NaOH/urea solvent and adding 1 mL aliquot starch solution drop-wisely into 10 mL absolute ethanol which was continuously stirred. The resulting mixture was then centrifuged and the supernatant was removed to obtain the regenerated starch nanoparticles, which were rinsed with absolute ethanol to remove NaOH and urea [15].

Citric acid treatment of starch nanoparticles

Citric acid (5 g) and sodium hypophosphite (1 g) were dissolved in 6 mL of water and the starch nanoparticle was added to the citric acid solution and mixed vigorously with a glass rod. The mixture

was placed in an oven to dehydrate at 100 °C for 30 minutes to eradicate the surface moisture and form a stable citric acid coat on the starch nanoparticles. The oven temperature was increased to 120 °C and the material was allowed to react further for 4 hours. The nano-starch citrate was slurried in water for 30 minutes and adjusted to pH 2 using acetic acid, then later filtered, washed with water and air-dried (7).

RESULTS AND DISCUSSION

This method uses the solubility difference and precipitation equilibria of starch-urea and starch-ethanol complex to synthesize starch nanoparticles. The starch dissolves to produce a temporary starch-urea complex in the alkaline urea solution and is immediately precipitated in absolute ethanol as nanoparticles.

FTIR Analyses

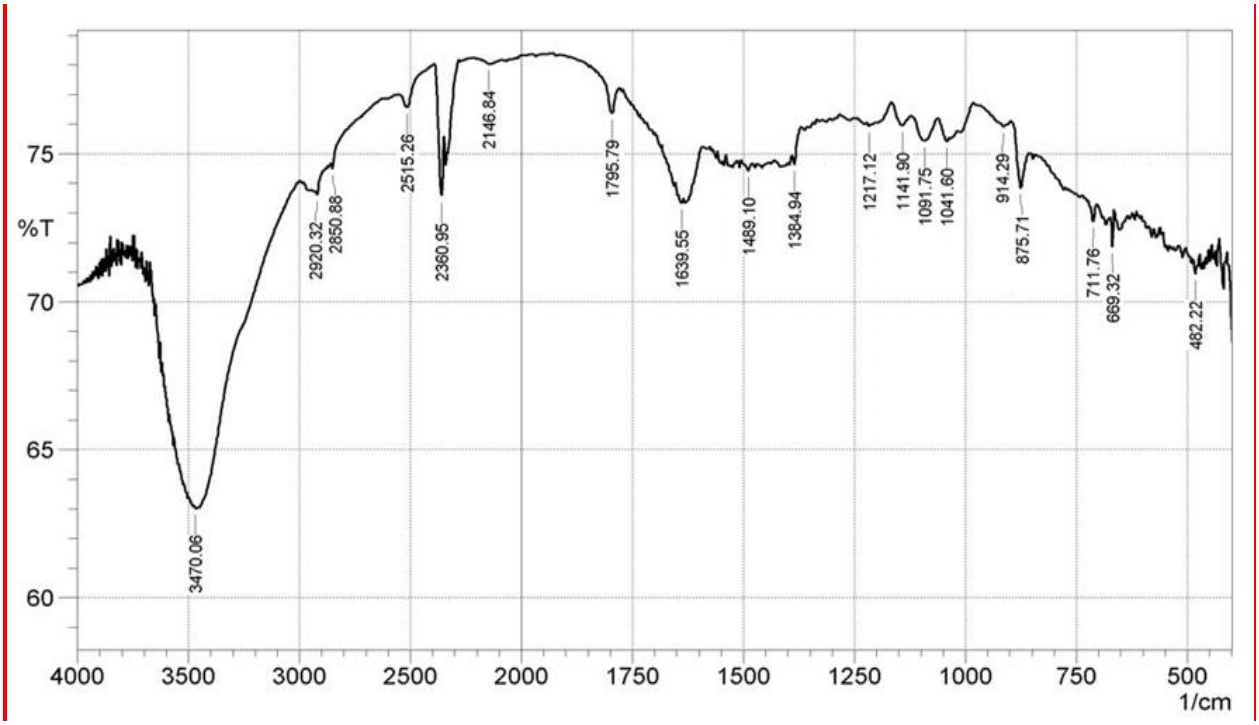

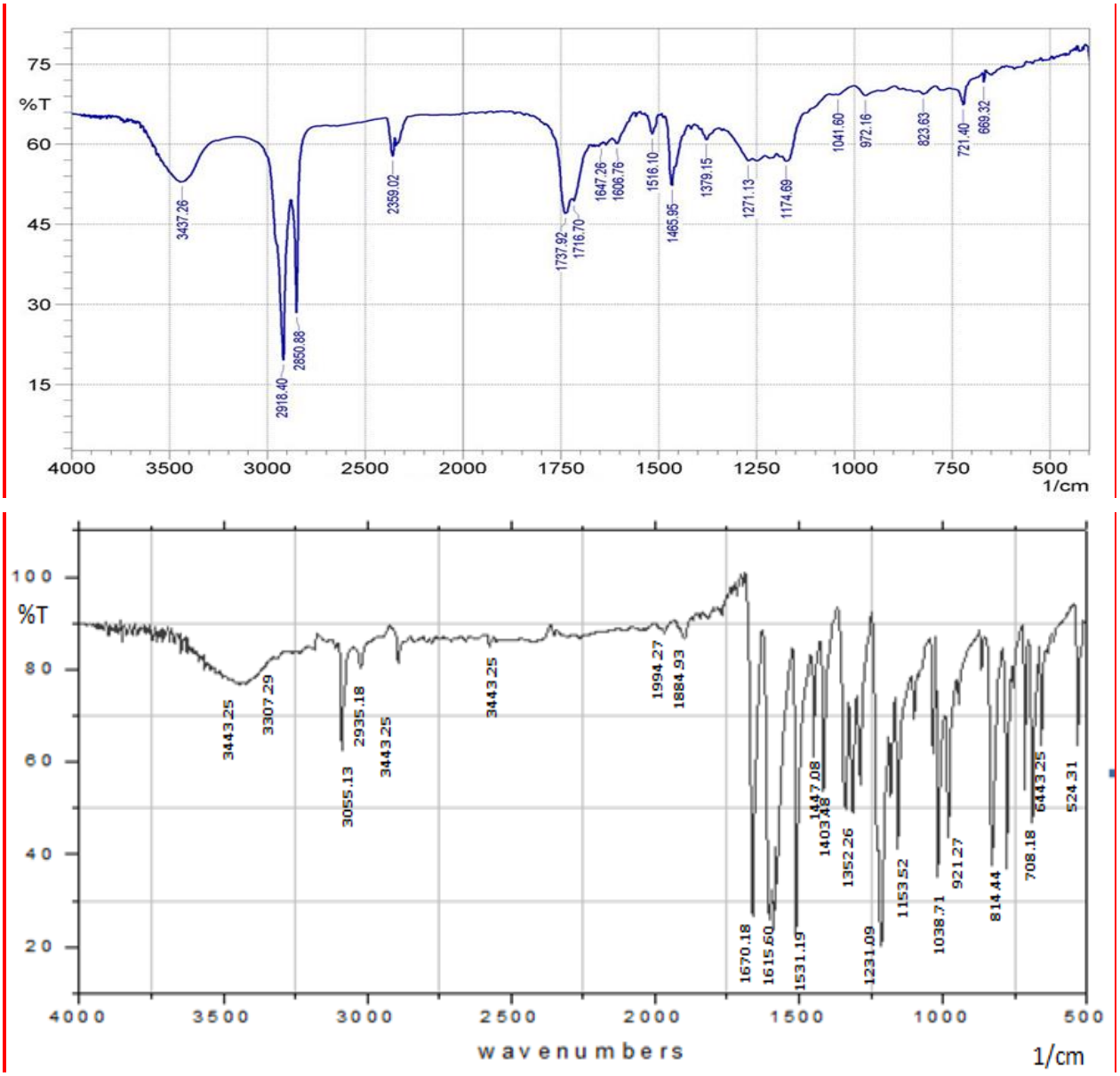

Figure 1: FTIR of starch, nano starch and starch citrate nanoparticles (from top to down)

The transmittance peaks at 3470 cm^{-1}, 2920 cm^{-1}, and 2850 cm^{-1} represents the O-H, symmetric and asymmetric C-H groups respectively while the carbonyl functional group in the starch is shown at 1639 cm^{-1}. The presence of the anhydroglucose glycosidic bond (C-O-C) is revealed at 914 cm^{-1} while the peak at 1091 cm^{-1} confirms the C-O functional group. Several bending vibrations of the C-H group are seen at 1041, 875 and 711 cm^{-1}. The presence of transmittance peaks of typical functional groups at reduced wavenumbers and the disappearance of some bands at the fingerprint region confirms the formation of starch nanoparticles (23). The reductions include 3470 to 3437 cm^{-1} for hydroxyl functional group, 2920 to 2850 for C-H stretching vibrations, 2515 to 2359 cm^{-1} for internal hydroxyl group vibrations, 1795 to 1737 for carbonyl group in starch to the synthesized nanostarch (15). Although some bending vibrations like 1384 to 1465 for C-H and 1217 to 1271

cm^{-1} for OH revealed a minimal increase in wavenumbers. The nanostarch citrate spectrum contain additional transmittance peaks at 1670 cm^{-1} for the C=O of polysaccharide esters, 3307 cm^{-1} for OH of citric acid and several bands for C-H wagging and scissoring which are as result of the citric acid treatment [20].

SEM and TEM Analyses

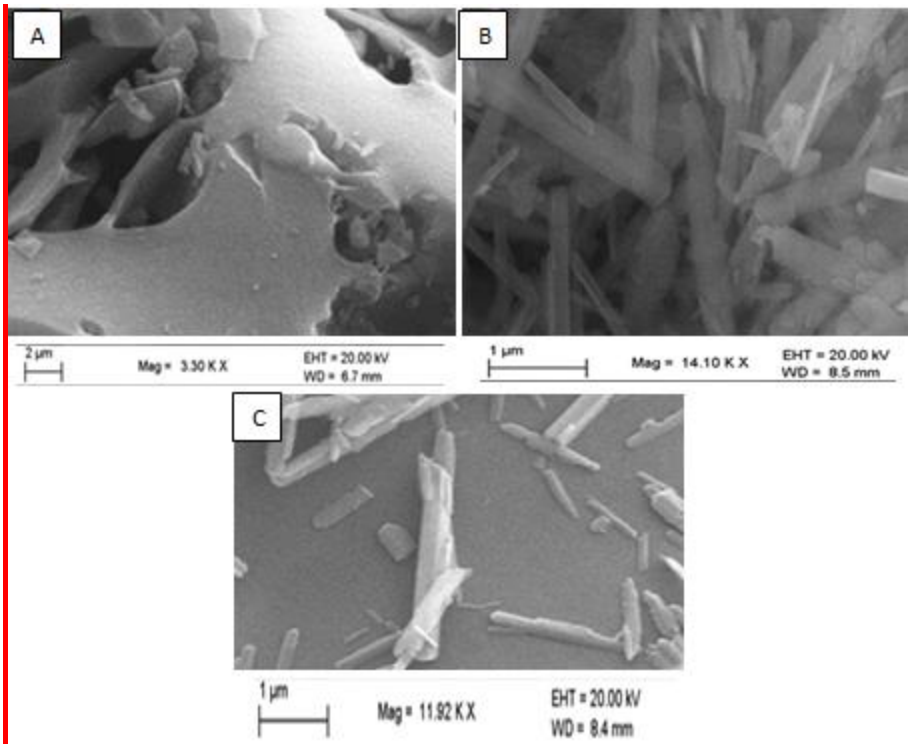

Figure 2: SEM of (a) starch, (b) nano starch and (c) starch citrate nanoparticles.

The scanning electron microscope (SEM) images of the starch shows a non-smooth surface in which a part appears concrete and the other parts appear broken. The surface of the starch appears tightly closed and no pores or gaps could be seen. After the size reduction to the nano level, the SEM shows an aggregate of starch nanoparticles, which looks disorderly arranged. The major difference this picture has with that of the normal starch is the presence of spaces in between these aggregated nanoparticles (13). The nanostarch citrate appears more rod like or cylindrical and shows little or no aggregation, this property coupled with its thermal stability makes it a good stabilizer in nano or micro emulsions of food, detergents and even paint products (21).

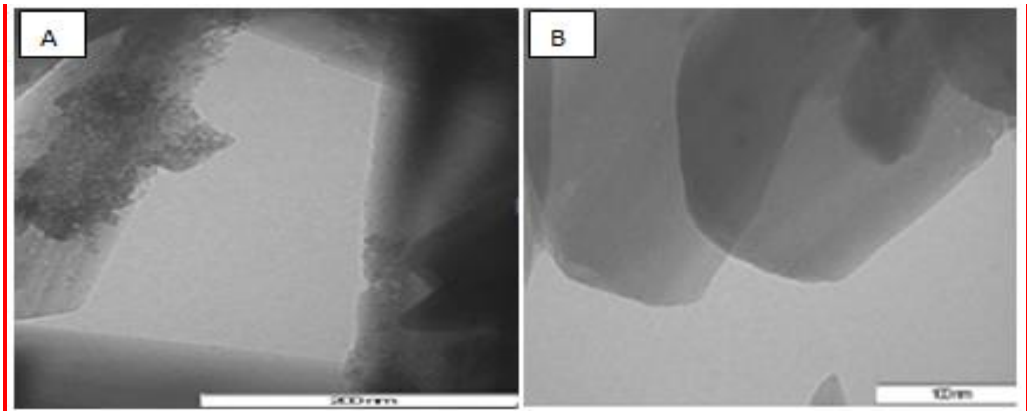

Figure 3: TEM of (a) nano starch and (b) starch citrate nanoparticles.

The transmission electron images (TEM) further confirm the synthesis of starch nanoparticles and its aggregated form while the image for the citric acid treated form appear less conglomerated and rod-like. The reason for this less aggregation might be as a result of the overall negative charge that develops from the surface citrate charges which also tend to stabilize and reduce agglomeration of these nanoparticles by electron-electron repulsion charge effect (21).

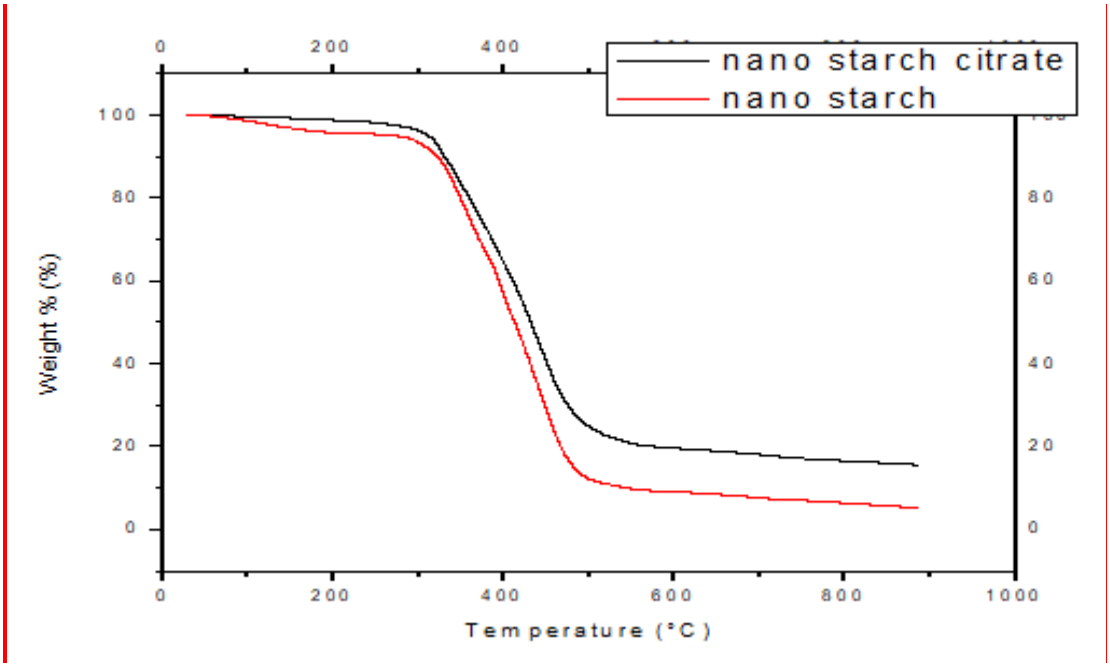

Figure 4: TGA of nano starch and starch citrate nanoparticles.

In Figure 4 above, the effect of citric acid treatment on thermal stability of nanostarch was investigated by thermogravimetric analysis. From the TGA curve, a single-step thermal degradation was observed from 180 to 400 °C for the nano starch with about 93% weight loss. However, the nanostarch citrate showed better thermal stability with its single step thermal degradation observed at 240 to 410 °C and percentage weight loss of about 89% (24). The T_{max} which is the temperature when maximum weight loss occurs in the thermal degradation of these starch biopolymers can also

be read from the TGA curves - 280°C for the nanostarch and 310°C for the nanostarch citrate (19). The improvement in the thermal stability can be assigned to the O-H substitution by citrate groups after the citric acid treatment.

CONCLUSION

The derivatization of starch and its applications was well explained in this paper. Although pectins are already been used as stabilizers, starch nanorods are new biopolymers which finds applications in emulsion stabilization. They are thermodynamically stable and have good morphological structure which fits this purpose.

REFERENCES

1. Ma X, Jian R, Chang PR, Yu J. Fabrication and Characterization of Citric Acid-Modified Starch Nanoparticles/Plasticized-Starch Composites. Biomacromolecules. 2008 Nov 10;9(11):3314–20.

2. Yu J, Wang N, Ma X. Fabrication and Characterization of Poly(lactic acid)/Acetyl Tributyl Citrate/Carbon Black as Conductive Polymer Composites. Biomacromolecules. 2008 Mar;9(3):1050–7.

3. Santander-Ortega MJ, Csaba N, Alonso MJ, Ortega-Vinuesa JL, Bastos-González D. Stability and physicochemical characteristics of PLGA, PLGA:poloxamer and PLGA:poloxamine blend nanoparticles. Colloids and Surfaces A: Physicochemical and Engineering Aspects. 2007 Mar;296(1–3):132–40.

4. Santander-Ortega MJ, Stauner T, Loretz B, Ortega-Vinuesa JL, Bastos-González D, Wenz G, et al. Nanoparticles made from novel starch derivatives for transdermal drug delivery. Journal of Controlled Release. 2010 Jan 4;141(1):85–92.

5. López-León T, Elaïssari A, Ortega-Vinuesa JL, Bastos-González D. Hofmeister Effects on Poly(NIPAM) Microgel Particles: Macroscopic Evidence of Ion Adsorption and Changes in Water Structure. ChemPhysChem. 2007 Jan 8;8(1):148–56.

6. Chivrac F, Pollet E, Schmutz M, Avérous L. New Approach to Elaborate Exfoliated Starch-Based Nanobiocomposites. Biomacromolecules. 2008 Mar;9(3):896–900.

7. Enturi V, Chowdary BY, Chowdary K. Enhancement of dissolution rate and formulation development of irbesartan tablets by employing starch phosphate: A new modified starch. Asian Journal of Pharmaceutics (AJP): Free full text articles from Asian J Pharm. 2014;8(3).

8. Jivraj M, Martini LG, Thomson CM. An overview of the different excipients useful for the direct compression of tablets. Pharmaceutical Science & Technology Today. 2000 Feb;3(2):58–63.

9. Wepner B, Berghofer E, Miesenberger E, Tiefenbacher K, N. K. Ng P. Citrate Starch — Application as Resistant Starch in Different Food Systems. Starch - Stärke. 1999 Oct;51(10):354–61.

10. Chin SF, Pang SC, Tay SH. Size controlled synthesis of starch nanoparticles by a simple nanoprecipitation method. Carbohydrate Polymers. 2011 Oct;86(4):1817–9.

11. Pang SC, Chin SF, Tay SH, Tchong FM. Starch–maleate–polyvinyl alcohol hydrogels with controllable swelling behaviors. Carbohydrate Polymers. 2011 Feb;84(1):424–9.

12. Kim J-Y, Lim S-T. Preparation of nano-sized starch particles by complex formation with n-butanol. Carbohydrate Polymers. 2009 Mar;76(1):110–6.

13. Loftsson T, Másson M, Brewster ME. Self-Association of Cyclodextrins and Cyclodextrin Complexes. Journal of Pharmaceutical Sciences. 2004 May;93(5):1091–9.

14. Rondeau-Mouro C, Bail PL, Buléon A. Structural investigation of amylose complexes with small ligands: inter- or intra-helical associations? International Journal of Biological Macromolecules. 2004 Oct;34(5):251–7.

15. Shi A, Li D, Wang L, Li B, Adhikari B. Preparation of starch-based nanoparticles through high-pressure homogenization and miniemulsion cross-linking: Influence of various process parameters on particle size and stability. Carbohydrate Polymers. 2011 Feb 1;83(4):1604–10.

16. Veiseh O, Gunn JW, Zhang M. Design and fabrication of magnetic nanoparticles for targeted drug delivery and imaging. Advanced Drug Delivery Reviews. 2010 Mar;62(3):284–304.

17. Demitri C, Del Sole R, Scalera F, Sannino A, Vasapollo G, Maffezzoli A, et al. Novel superabsorbent cellulose-based hydrogels crosslinked with citric acid. Journal of Applied Polymer Science. 2008 Nov 15;110(4):2453–60.

18. Fujioka R, Tanaka Y, Yoshimura T. Synthesis and properties of superabsorbent hydrogels based on guar gum and succinic anhydride. Journal of Applied Polymer Science. 2009 Oct 5;114(1):612–6.

19. Salam A, Pawlak JJ, Venditti RA, El-tahlawy K. Synthesis and Characterization of Starch Citrate−Chitosan Foam with Superior Water and Saline Absorbance Properties. Biomacromolecules. 2010 Jun 14;11(6):1453–9.

20. Chang PR, Yu J, Ma X. Preparation of porous starch and its use as a structure-directing agent for production of porous zinc oxide. Carbohydrate Polymers. 2011 Jan;83(2):1016–9.

21. Abbas S, Bashari M, Akhtar W, Li WW, Zhang X. Process optimization of ultrasound-assisted curcumin nanoemulsions stabilized by OSA-modified starch. Ultrasonics Sonochemistry. 2014 Jul;21(4):1265–74.

22. Karadag A, Yang X, Ozcelik B, Huang Q. Optimization of Preparation Conditions for Quercetin Nanoemulsions Using Response Surface Methodology. Journal of Agricultural and Food Chemistry. 2013 Mar 6;61(9):2130–9.

23. Manoi K, Rizvi SSH. Physicochemical characteristics of phosphorylated cross-linked starch produced by reactive supercritical fluid extrusion. Carbohydrate Polymers. 2010 Jul;81(3):687–94.

24. Ghosh V, Mukherjee A, Chandrasekaran N. Ultrasonic emulsification of food-grade nanoemulsion formulation and evaluation of its bactericidal activity. Ultrasonics Sonochemistry. 2013 Jan;20(1):338–44.